

Galactic Stellar Populations in the Era of SDSS and Other Large Surveys

ŽELJKO IVEZIĆ

*Department of Astronomy, University of Washington, Box 351580, Seattle, WA
98195*

TIMOTHY C. BEERS

*National Optical Astronomy Observatory, Tucson, AZ, 85719, Department of
Physics & Astronomy and JINA: Joint Institute for Nuclear Astrophysics,
Michigan State University, East Lansing, MI 48824*

MARIO JURIĆ

*Harvard-Smithsonian Center for Astrophysics, 60 Garden Street, Cambridge,
MA 02138; Hubble Fellow*

Key Words methods: data analysis – stars: statistics – Galaxy: disk, halo,
stellar content, structure, interstellar medium

Abstract

Studies of stellar populations, understood to mean collections of stars with common spatial,

kinematic, chemical, and/or age distributions, have been reinvigorated during the last decade by the advent of large-area sky surveys such as SDSS, 2MASS, RAVE, and others. We review recent analyses of these data that, together with theoretical and modeling advances, are revolutionizing our understanding of the nature of the Milky Way, and galaxy formation and evolution in general. The formation of galaxies like the Milky Way was long thought to be a steady process leading to a smooth distribution of stars. However, the abundance of substructure in the multi-dimensional space of various observables, such as position, kinematics, and metallicity, is by now proven beyond doubt, and demonstrates the importance of mergers in the growth of galaxies. Unlike smooth models that involve simple components, the new data reviewed here clearly exhibit many irregular structures, such as the Sagittarius dwarf tidal stream and the Virgo and Pisces overdensities in the halo, and the Monoceros stream closer to the Galactic plane. These recent developments have made it clear that the Milky Way is a complex and dynamic structure, one that is still being shaped by the merging of neighboring smaller galaxies. We also briefly discuss the next generation of wide-field sky surveys, such as SkyMapper, Pan-STARRS, Gaia, and LSST, which will improve measurement precision manyfold, and comprise billions of individual stars. The ultimate goal, development of a coherent and detailed story of the assembly and evolutionary history of the Milky Way and other large spirals like it, now appears well within reach.

CONTENTS

INTRODUCTION	4
<i>The Big Picture: Structure Formation and</i>	
<i>Near-field Cosmology</i>	4
<i>Stellar Populations: Definition and Role</i>	6
<i>Observations: Photometry, Spectroscopy, Astrometry</i>	9
THE ADVENT OF LARGE-AREA DIGITAL SKY SURVEYS	12
<i>The SDSS Imaging and Spectroscopic Surveys</i>	13
<i>The SDSS-POSS Proper-Motion Survey</i>	15
<i>The 2MASS Imaging Survey</i>	16

<i>The RAVE Spectroscopic Survey</i>	16
OVERVIEW OF THE STATE-OF-THE-ART A DECADE AGO	18
<i>What is the nature of the halo MDF?</i>	19
<i>The ELS vs. SZ model of halo formation</i>	20
<i>What is the shape of the halo?</i>	20
<i>Are the thin and thick disk distinct entities?</i>	21
<i>Is the metal-weak thick disk real?</i>	21
<i>Are there stellar streams other than Sagittarius?</i>	21
WHAT DID WE LEARN DURING THE LAST DECADE?	22
<i>Separation of the Main Structural Components</i>	23
THE MILKY WAY DISK	26
<i>The Holy Grail for Thin-Thick Disk Decomposition: $[\alpha/Fe]$</i>	28
<i>Comparisons of Observations with Disk Formation Models</i>	36
<i>A Summary of Recent Disk Studies</i>	41
THE MILKY WAY HALO	42
<i>The Smooth Halo Behavior as Probed by Main-Sequence Stars</i>	44
<i>Beyond a Simple Power Law: One Halo, Two Halos, Many Halos?</i>	47
<i>What is the Nature of the Outer Halo?</i>	52
<i>Streams and Other Substructure</i>	55
UNANSWERED QUESTIONS	61
THE ROAD AHEAD	63
<i>SDSS APOGEE Survey</i>	63
<i>The LAMOST Galactic Surveys</i>	64
<i>SkyMapper, Pan-STARRS, and the Dark Energy Survey</i>	65
<i>Gaia</i>	67
<i>LSST</i>	68

1 INTRODUCTION

1.1 The Big Picture: Structure Formation and Near-field Cosmology

The current cosmological paradigm states that the Universe had its beginning in the Big Bang. Galaxies, the fundamental (luminous) building blocks of the Universe, began forming relatively soon after this event (no more than a few Gyr). A major objective of modern astrophysics is to understand when and how galaxies formed, and how they have evolved since. Our own galaxy, the Milky Way, provides a unique opportunity to study a galaxy in exquisite detail, by measuring and analyzing the properties of large samples of individual stars. Characterization of the stellar populations of the Milky Way provides clues about galaxy formation and evolution that cannot be extracted from observations of distant galaxies alone. Indeed, it is not possible to tell a coherent story of the formation of the first stars and galaxies without understanding the nature of the stellar populations of the Milky Way.

In the canonical model of Milky Way formation (Eggen, Lynden-Bell & Sandage 1962) the Galaxy began with a relatively rapid ($\sim 10^8$ yr) radial collapse of the initial protogalactic cloud, followed by an equally rapid settling of gas into a rotating disk. The ELS scenario readily explained the origin and general structural, kinematic, and metallicity correlations of observationally identified populations of field stars, and implied a smooth distribution of stars observable today. The predictions of the ELS scenario were quantified by the Bahcall & Soneira (1980) and Gilmore, Wyse & Kuijken (1989) models, and reviewed in detail by, e.g.,

Majewski (1993). In these smooth models, the Milky Way in the relatively nearby region (within ~ 5 kpc) is usually modeled by three discrete components described by fairly simple analytic expressions: the thin disk, the thick disk, and the halo. The other known components, the bulge and the bar, are not expected to directly contribute to the stellar populations in this local region.

However, for some time, starting with the pioneering work of Searle & Zinn (1978), and culminating with recent discoveries of complex substructure in the distribution of the Milky Way's stars, this standard view has experienced difficulties. Unlike the smooth models with simple components that have been used on local scales, new data on larger scales indicate the presence of much more irregular structures, such as the Sgr dwarf tidal stream and the Virgo and Pisces overdensities in the halo, and the Monoceros stream closer to the Galactic plane. Recent observational developments, based on accurate large-area sky surveys, have made it abundantly clear that the Milky Way is a complex and dynamic structure that is still being shaped by the infall (merging) of neighboring smaller galaxies. Numerical simulations suggest that this merger process plays a crucial role in establishing the structure and motions of stars within galaxies, and is a generic feature of current cosmological models (Brook et al. 2005; Bullock & Johnston 2005; Font et al. 2011; Governato et al. 2004, 2007; Johnston et al. 2008; Sommer-Larsen, Götz & Portinari 2003; Steinmetz & Navarro 2002).

The main purpose of this review is to summarize some of the recent observational progress in Milky Way studies, and the paradigm shifts¹ in our understanding of galaxy formation and evolution resulting from this progress. This

¹This phrase was introduced by Thomas Kuhn, who apparently overused it (P. Yoachim, priv. comm.). Here, it implies a change in the basic assumptions about galaxy formation, from the smooth collapse model to the galaxy mergers scenario.

review is focused on only a few studies, based mostly on data collected by the Sloan Digital Sky Survey² described by York et al. (2000, hereafter SDSS), and does not represent an exhaustive overview of all the progress made during the last decade. One of our goals is to illustrate novel analysis methods enabled by new datasets. We begin with a brief overview of methodology, and of a few major datasets, and then describe the main observational results. We conclude by discussing some of the unanswered questions, and observational prospects for the immediate future.

1.2 Stellar Populations: Definition and Role

In astronomy, the term stellar populations is often associated with Populations I, II, and III, although the precise meanings of these populations has changed over time. These stellar classes generally represent a sequence of decreasing metallicity and increasing age. Here, we will use the term “stellar population” to mean any collection of stars with common spatial, kinematic, chemical, luminosity, and/or age distributions. For example, a sample of red-giant stars selected using appropriate observables and selection criteria is considered a population, although such a sample can include both Population I and Population II stars. Similarly, we will often consider populations of “disk” and “halo” stars, or samples selected from a narrow color range. In summary, any sample of stars that share some common property that is appropriate for mapping the Galaxy in the space of various observables is hereafter considered to be a “population”.

Most studies of the Milky Way can be described as investigations of the stellar distribution, or statistical behavior of various stellar populations, in the seven-

²www.sdss.org

dimensional (7-D) phase space spanned by the three spatial coordinates, three velocity components, and metallicity (of course, the abundances of individual chemical elements can be treated as additional coordinates; this will be a key ingredient for progress in the next decade). Depending on the quality, quantity, and diversity of the data, such studies typically concentrate on only a limited region of this 7-D space (e.g., the solar neighborhood, pencil beam surveys, kinematically biased surveys), or consider only marginal distributions (e.g., the number density of stars irrespective of their metallicity or kinematics, proper-motion surveys without metallicity or radial-velocity information). The primary driver of the substantial progress in our knowledge of the Milky Way over the last decade is the ability of modern sky surveys to deliver the data required for determining the phase-space coordinates for unprecedented numbers of faint stars over large areas of the sky. For example, in less than two decades the observational material for kinematic mapping has progressed from the first pioneering studies based on only a few hundred objects (Majewski 1992), to over a thousand objects (Chiba & Beers 2000), to the massive datasets including millions of stars reviewed here.

The availability of large stellar samples enables detailed studies of various distributions, including determination of the distributions' shape, rather than considering only low-order statistical measures, as is done for small samples. Deviations from Gaussian shapes often encode more information about the history of galaxy assembly than the distribution's mean and dispersion. The large samples are especially important for considering multi-variate distributions (as opposed to one-dimensional marginal distributions), as the so-called "curse of dimension-

ality³” prevents their accurate determination with small samples.

In addition to increasing the sample size, the ability to detect faint stars is crucial for extending the sample distance limit. With SDSS, it has become possible to detect even main-sequence (dwarf) stars to a distance limit exceeding 10 kpc, and thus to probe both the disk and halo populations within the same dataset. The advantage of carrying out analyses of multiple populations using stellar probes of similar intrinsic properties is difficult to overstate. By way of comparison, the main-sequence stars in the Hipparcos sample (Perryman et al. 1997) only explore the volume within ~ 100 pc of the Sun. The primary advantage of main-sequence stars over probes such as RR Lyrae stars, blue horizontal-branch (BHB) stars, and red-giant stars for studying Galactic populations is that they are much more numerous (on the order of a thousand times more than these other populations summed together), and thus enable a substantially higher spatial resolution of the resulting phase-space maps (assuming a fixed number of stars per multi-dimensional pixel in phase space, and neglecting the intrinsic limit on spatial resolution set by the distance precision). Of course, these other probes are still valuable, because they can be used to explore the Galaxy to a larger distance limit than obtainable with main-sequence stars alone.

A theme common to most of the studies reviewed here is the use of photometric parallax relations to estimate stellar distances, followed by the subsequent direct mapping of various distributions using large samples of stars. This mapping approach does not require a-priori model assumptions, and instead constructs multi-dimensional distribution maps first, and only then looks for structure in the

³When the problem dimensionality is high, the probability for a data point to belong to a multi-dimensional bin becomes small, and the bins become sparsely populated if the sample is not sufficiently large.

maps and compares them to Galactic models. A key observational breakthrough that made this approach possible was the availability of accurate multi-band optical photometry to a faint flux limit over a large area of sky, delivered by SDSS, as discussed below.

1.3 Observations: Photometry, Spectroscopy, Astrometry

In order to determine the coordinates of a star in 7-D phase space, a variety of astronomical techniques must be used. As always, the most crucial quantity to measure is stellar distance. The largest sample of stars with trigonometric distances, obtained by the Hipparcos survey, is too shallow (and too small) to complement deep surveys such as SDSS and 2MASS (see below for an overview of these surveys). Until the all-sky Gaia survey measures trigonometric distances for about a billion stars brighter than $V = 20$ (see §8.4), various photometric methods need be employed in order to estimate distances. A common aspect of these methods is that the luminosity (i.e., absolute magnitude) of a star is determined by constraints derived from its color measurements, then its distance is determined from the observed difference between its absolute and apparent magnitude. For certain populations, for example RR Lyrae stars, a good estimate of absolute magnitude is obtained as a simple constant (with some metallicity dependence); for other populations, such as main-sequence stars, the absolute magnitude depends on both effective temperature and metallicity, and sometimes on age (or surface gravity) as well. A photometric parallax method for main-sequence stars is described below.

The most accurate measurements of stellar metallicity are based on spectroscopic observations (but see below for a method of estimating metallicity using

photometric data alone). Spectroscopic measurements are especially important when studying the extremely low end of the metallicity distribution function, where photometric methods become insensitive. In addition to measuring chemical composition, spectroscopic observations enable radial-velocity measurements. The two largest existing stellar spectroscopic surveys are SDSS and RAVE (see the next section).

To measure all three components of the space-velocity vector, precise astrometric observations are also required. The projection of the space-velocity vector into the tangent plane (i.e., perpendicular to the radial-velocity component) is measured using proper motion (the astrometric position shift per unit time), which can be combined with the distance estimate to yield the space velocity. The proper-motion measurements place an additional constraint on observations; at least two (ideally, widely temporally separated) astrometric epochs must be available.

Therefore, multi-color imaging, multi-epoch astrometry, and spectroscopy are required for measuring the coordinates of a star in the 7-D position-velocity-metallicity phase space. It is the advent of massive and accurate imaging and spectroscopic surveys that delivered such measurements for large and relatively unbiased samples of stars, and thus enabled major progress in Milky Way phase-space mapping during the last decade.

1.3.1 A PHOTOMETRIC PARALLAX METHOD FOR MAIN-SEQUENCE STARS

In order to estimate distances to main-sequence stars with an accuracy of 10-20% through the use photometric parallax relations, multi-band optical photometry accurate to several percent (i.e., to several hundredths of a magnitude) is required. This stringent requirement comes from the steepness of the color-luminosity rela-

tion (the derivative of the absolute magnitude in the SDSS r -band with respect to the $g - i$ color reaches ~ 10 mag/mag at the blue end), and is the main reason why it was not possible to use this method with large sky surveys prior to SDSS.

Using globular cluster data obtained in the SDSS photometric system, Ivezić et al. (2008b, hereafter Ivezić08) derived a polynomial expression for the absolute magnitude of main-sequence stars in the r -band as a function of their $g - i$ color and metallicity (see their eqs. A2 and A7). The accuracy of the resulting magnitudes is in the range 0.1-0.2 mag (Ivezić08; Sesar, Ivezić & Jurić 2008), and the method enables studies of the ~ 100 pc to ~ 10 kpc distance range when used with SDSS data. The ability to estimate distances to main-sequence stars with sufficient accuracy using only SDSS photometry was crucial for wide-angle panoramic mapping of the Galaxy to a distance limit 100 times farther than possible with the Hipparcos data alone.

1.3.2 A PHOTOMETRIC METALLICITY METHOD FOR MAIN-SEQUENCE STARS

Stellar metallicity, together with effective temperature and surface gravity, is one of the three main parameters that affect the observed spectral energy distribution of most stars. In addition to being an informative observable for deciphering the Milky Way's chemical history (e.g., Majewski 1993; Freeman & Bland-Hawthorn 2002; Helmi 2008; Majewski 2010; and references therein), knowledge of stellar metallicity is crucial for accurate estimates of distances using photometric parallax relations.

The most accurate measurements of stellar metallicity are based on spectroscopic observations. However, despite recent progress in the availability of at least low-resolution digital stellar spectra (approaching a million!), the number of stars detected in imaging surveys is still vastly larger. In addition to generally provid-

ing better sky and depth coverage than spectroscopic surveys, imaging surveys obtain essentially complete flux-limited samples of stars. These simple selection criteria are advantageous when studying Galactic structure, compared with the complex targeting criteria that are (by necessity) often used for spectroscopic samples.

As first suggested by Schwarzschild, Searle & Howard (1955), the depletion of metals in a stellar atmosphere has a detectable effect on the emergent flux, in particular in the blue spectral region where the density of metallic absorption lines is highest (Beers & Christlieb 2005, and references therein). Recent analysis of SDSS data by Ivezić08 demonstrated that for blue F- and G-type main-sequence stars, a metallicity estimate accurate to ~ 0.2 dex can be derived from the $u - g$ color. They derived a polynomial expression that maps the measured $u - g$ vs. $g - r$ color space to effective temperature and metallicity ($[Fe/H]$) (for updated coefficients see Bond et al. 2010, hereafter Bond10). This transformation, applicable to stars with $0.2 < g - r < 0.6$, was calibrated using $\sim 100,000$ stars with available spectroscopic metallicity determinations, and has errors in the range 0.2-0.3 dex when used with SDSS data (for stars in the range⁴ $-2 < [Fe/H] < +0.3$; for more details see Ivezić08 and Bond10). Although applicable only within a restricted color range, this calibration has enabled the construction of metallicity maps using millions of stars, as discussed further below.

2 THE ADVENT OF LARGE-AREA DIGITAL SKY SURVEYS

Major advances in our understanding of the Milky Way have historically arisen from dramatic improvements in our ability to “see”, as vividly exemplified by

⁴This metallicity range includes $\sim 99\%$ of all stars in the Milky Way.

Galileo resolving the Milky Way disk into individual stars. Progressively larger telescopes have been developed over the past century, but until recently most astronomical investigations have focused on small samples of objects because the largest telescope facilities typically have rather small fields of view, and those with large fields of view could not detect very faint sources. Over the past two decades, however, astronomy moved beyond the traditional observational paradigm and undertook large-scale digital sky surveys, such as SDSS and the Two Micron All Sky Survey⁵ (Skrutskie et al. 2006, hereafter 2MASS). This observational progress, based on advances in telescope construction, detectors, and above all, information technology, has had a dramatic impact on nearly all fields of astronomy, including studies of the structure of the Milky Way. Here we briefly overview the characteristics of the most massive recent datasets.

2.1 The SDSS Imaging and Spectroscopic Surveys

The SDSS is a digital photometric and spectroscopic survey which covered over one quarter of the Celestial Sphere in the North Galactic cap (approximately, $b > 30^\circ$), and produced a smaller area ($\sim 300 \text{ deg}^2$) but much deeper survey in the Southern Galactic hemisphere, along the Celestial Equator (Aihara et al. 2011, and references therein). The recent Data Release 8 has a sky coverage of about $14,600 \text{ deg}^2$, and includes photometric measurements for 469 million unique objects (approximately half are stars). The completeness of the SDSS catalogs for point sources is $\sim 99\%$ at the bright end, dropping to 95% at an r -band magnitude of ~ 22 . The wavelength coverage of the SDSS photometric system ($ugriz$, with effective wavelengths from 3540 \AA to 9250 \AA), and photometry accurate

⁵www.ipac.caltech.edu/2mass/

to ~ 0.02 mag, have enabled photometric parallax and metallicity estimates for many millions of stars. For comparison, the best large-area optical sky survey prior to SDSS, the photographic Palomar Observatory Sky Survey, had only two photometric bands, several times larger photometric errors, and was limited by uncertain zero points that varied from plate-to-plate (Sesar et al. 2006).

In addition to its imaging survey data, SDSS has obtained well over half a million stellar spectra, many as part of the Sloan Extension for Galactic Understanding and Exploration (SEGUE; Yanny et al. 2009), and its continuation SEGUE-2, sub-surveys carried out during the first (SDSS-II) and second (SDSS-III; Eisenstein et al. 2011) extensions of the SDSS project. These spectra have wavelength coverage 3800–9200 Å and spectral resolving power $R \sim 2000$, with a typical signal-to-noise ratio per 150 km s⁻¹ resolution element of > 30 at $r \sim 18.5$, and ~ 3 at $r \sim 20$. SDSS stellar spectra are of sufficient quality to provide robust and accurate stellar parameters, such as effective temperature, surface gravity, and metallicity (parameterized as $[Fe/H]$). These publicly available parameters are estimated using a variety of methods implemented in an automated pipeline (Beers et al. 2006, the SEGUE Stellar Parameters Pipeline, SSPP). A detailed discussion of these methods and their performance can be found in Papers I-V of the SSPP series (Allende Prieto et al. 2008, Lee et al. 2011a, 2008a,b, Smolinski et al. 2011). Based on a comparison with high-resolution abundance determinations, they demonstrate that the combination of spectroscopy and photometry from SDSS is capable of delivering estimates of T_{eff} , $\log(g)$, and $[Fe/H]$ accurate to 200 K (3%), 0.3 dex, and 0.2 dex, respectively. Random errors for the radial-velocity measurements are a function of spectral type, but are usually < 5 km s⁻¹ for stars brighter than $r \sim 18$, rising to ~ 20 km s⁻¹ for stars

with $r \sim 20$ (Pourbaix et al. 2005, Yanny et al. 2009). Lee et al. (2011a) demonstrate that SDSS spectra are of sufficient quality to also determine $[\alpha/Fe]$ with errors below 0.1 dex (for stars with temperatures in the range 4500-7000 K and sufficient signal-to-noise ratios). The distribution of SDSS stars with available spectroscopic estimates of atmospheric parameters in the $\log(g)$ vs. color plane is shown in Figure 1.

2.2 The SDSS-POSS Proper-Motion Survey

The time difference of about half a century between the Palomar Observatory Sky Survey (POSS) and the SDSS imaging observations provides an excellent baseline to measure proper motions for tens of millions of stars to faint brightness levels. Munn et al. (2004) addressed the problem of large systematic astrometric errors in the POSS catalogs by recalibrating the USNO-B catalog (Monet et al. 2003), using the positions of galaxies measured by SDSS. As a result of this calibration, the SDSS-POSS proper-motion measurements are now available for about 100 million unresolved sources, most of them stars. This catalog also includes about 70,000 spectroscopically-confirmed SDSS quasars that were used to robustly estimate the proper-motion errors (Bond et al. 2010). The random errors increase from $\sim 3 \text{ mas yr}^{-1}$ at the bright end to $\sim 6 \text{ mas yr}^{-1}$ at $r \sim 20$ (the sample completeness limit), with systematic errors that are typically an order of magnitude smaller, and with very small variation across the sky (for a discussion of deviations from Gaussian error behavior, see Dong et al. 2011). Even for stars at distances of 1 kpc, the implied tangential velocity errors are as small as 10-20 km s^{-1} , and well matched to the SDSS radial velocity accuracy. This catalog represents a major improvement over previously available data sets both in size

and accuracy.

2.3 The 2MASS Imaging Survey

The 2MASS databases are derived from an all-sky near-IR photometric survey with limiting (Vega-based, 10σ) magnitudes of $J=15.8$, $H=15.1$, and $K=14.3$. The 2MASS point source catalog contains positional and photometric information for 471 million sources (mostly stars). The near-IR 2MASS colors are not as good as the optical SDSS colors for estimating photometric parallax and metallicity, because they only probe the Rayleigh-Jeans tail of the stellar spectral energy distribution. On the other hand, a major advantage of 2MASS over SDSS is the full sky coverage, and its ability to penetrate deeper through the interstellar dust in the Galactic plane. In addition, it is much easier to photometrically identify certain stellar populations using near-IR data than with optical data. For example, Majewski et al. (2003) have demonstrated that M-giant candidates color selected from the 2MASS database are extremely powerful probes of halo substructure out to ~ 100 kpc over the entire sky (these stars are practically impossible to robustly identify using SDSS photometry). For an analysis of the joint SDSS-2MASS stellar dataset, we refer the reader to Covey et al. (2007).

2.4 The RAVE Spectroscopic Survey

The Radial Velocity Experiment⁶ (RAVE) is a major new spectroscopic survey aiming to measure radial velocities and stellar atmosphere parameters (temperature, surface gravity, and metallicity) of up to one million stars using the Six Degree Field multi-object spectrograph on the 1.2m UK Schmidt Telescope of the

⁶www.rave-survey.aip.de

Anglo-Australian Observatory (Steinmetz et al. 2006). RAVE stars are selected from the magnitude range $9 < I < 12$, and represent a bright complement to the SDSS spectroscopic sample (Siebert et al. 2011). The wavelength range for the RAVE spectra (8410–8795 Å, in the region of the Ca II Triplet, with a spectral resolving power of $R \sim 8000$) includes a number of lines in addition to calcium, and should eventually provide reliable estimates of $[\alpha/Fe]$ for numerous stars, in addition to overall metallicity ($[Fe/H]$). The RAVE catalog of stellar elemental abundances (Boeche et al. 2011) includes estimates of abundances for Mg, Al, Si, Ca, Ti, Fe and Ni, with a mean error of ~ 0.2 dex, for some 36,000 stars.

The third RAVE data release includes radial-velocity data for $\sim 77,000$ stars and stellar parameters for $\sim 40,000$ stars (Siebert et al. 2011), but spectra are already collected for over 300,000 stars (Zwitter et al. 2010). With a radial-velocity error of about 2 km s^{-1} , the RAVE velocities are more accurate than those delivered by SDSS, and are well-suited for detailed kinematic studies of nearby disk stars (Ruchti et al. 2011). Proper motions (of varying accuracy) are available for most of the RAVE stars from other surveys, and model-based distance determinations accurate to $\sim 20\%$ are also available (Burnett et al. 2011, Zwitter et al. 2010).

The distances probed by RAVE stars range from ~ 300 pc (dwarfs) to $\sim 1\text{--}2$ kpc (giants), and thus the RAVE dataset “connects” the nearby Hipparcos sample and the more distant SDSS sample. Due to these distance limits, RAVE data are more relevant for disk than for halo investigations. However, the RAVE survey has demonstrated the ability to identify at least a limited number (hundreds in the present sample, eventually several thousand) of bright, very low-metallicity stars with $[Fe/H] < -2.0$, including a handful with metallicity as low as $[Fe/H] = -4.0$ (Fulbright et al. 2010). Bright very metal-poor stars are of

particular interest, since follow-up high-resolution spectroscopy can be obtained with relatively short integration times on 4m to 8m-class telescopes. In addition, the large-area nearly-contiguous coverage of RAVE survey (see Figure 2) is very useful for panoramic Galactic mapping.

3 OVERVIEW OF THE STATE-OF-THE-ART A DECADE AGO

Before discussing results concerning the nature of Galactic structure and stellar populations obtained during the last decade, we briefly review the state of related knowledge a decade ago. We concentrate on the spectroscopic surveys in existence at that time, and the questions they sought to address.

Circa 2000, there were two primary approaches in common use for the detection and analysis of significant numbers of stars with membership in the thick-disk and halo populations of the Galaxy. The first, essentially a continuation of the high-proper-motion based surveys pioneered by Sandage and colleagues, is exemplified by the work of Ryan & Norris (1991) and that of Carney et al. (1996), and references therein. Both of these works concentrated on members of the halo population, although stars from the disk system were certainly present in their samples as well. The second, which followed on the efforts of Norris (1986), was the assemblage (Beers et al. 2000) and analysis (Chiba & Beers 2000) of a large sample of non-kinematically selected stars with $[\text{Fe}/\text{H}] < -0.6$ (this metallicity limit was chosen to minimize the contribution of disk-system stars). It was considered of central importance (as it remains now) to contrast the derived properties of samples chosen with differing biases – the former on kinematics, and the latter on metallicity. For this reason, papers that followed commonly adopted the

halo metallicity distribution functions (MDFs) as derived from the kinematically selected samples, and the kinematics of the thick-disk and halo populations based on the non-kinematically selected samples. It is worth noting that, even prior to the results obtained by these two surveys, Freeman (1987) called attention to the puzzling differences in the trends of the derived halo rotation velocities and velocity dispersions as a function of declining metallicity for the extant kinematically vs. non-kinematically selected stars. Today, it seems likely that this puzzle may be resolved by the recognition that, even within the halo component, there exists a strong coupling between kinematics and metallicity that was not previously apparent.

The most pressing questions from a decade ago included the following, asked and answered (even if only partially) below. Answers to the above questions were essentially all limited by the relatively small numbers of stars with 7-D phase-space information then available, as well as by the troublesome selection biases that were known to exist in the tracer samples. Even so, some progress toward resolution of these issues was being made at the time.

3.1 What is the nature of the halo MDF?

What is the nature of the MDF for the halo population, and does it include significant numbers of stars with metallicities below $[Fe/H] \sim -3.0$?

Although the proper-motion-selected samples included only a handful of stars with $[Fe/H] < -3.0$, the objective-prism surveys that were the source of the lowest metallicity stars known at that time (e.g., Beers, Preston & Shectman 1992) included tens of stars below this metallicity. The inference could be made that, although stars of such low metallicity were rare compared to the more metal-rich

halo stars with $[Fe/H] \sim -1.5$, they did in fact exist in substantial numbers.

3.2 The ELS vs. SZ model of halo formation

Can the kinematics of the halo of the Galaxy be adequately described by the rapid collapse model of Eggen, Lynden-Bell & Sandage (1962), ELS, or did the observations require the more extended, chaotic assembly picture of Searle & Zinn (1978)?

One of the primary discriminants between the suggested galaxy formation models is the presence (or not) of halo stars with low orbital eccentricities, which might not be expected to be found in significant number if the ELS model was the correct interpretation. Papers published prior to Chiba & Beers (2000) did in fact identify such stars (e.g., Norris, Bessell & Pickles 1985), but only relatively few. The question was essentially resolved by the substantially larger numbers of low-metallicity, low-eccentricity halo stars discussed by Chiba & Beers (2000).

3.3 What is the shape of the halo?

What is the shape of the density profile of the stellar halo, and does it remain constant with increasing distance (and/or declining metallicity)?

A number of papers prior to 2000 (e.g., Hartwick 1987; Preston, Sheckman & Beers 1991) pointed out that the shape of the stellar halo density profile changes with Galactocentric distance, in the sense that it is relatively flattened in the inner region, and becomes substantially rounder in the outer region. This result was validated by inferences based on the kinematics of local halo stars carried out by Sommer-Larsen & Zhen (1990) and Chiba & Beers (2000).

3.4 Are the thin and thick disk distinct entities?

Is the disk system adequately modeled by the superposition of a thin-disk and thick-disk population, that is, are these two components demonstrably distinct from one another?

Although Norris & Ryan (1991) made the argument that a continuous extended disk configuration could be supported by the existing data at that time, Chiba & Beers (2000) claimed that the kinematics and abundances of thick-disk stars indicated that a distinct thick-disk component was the more likely interpretation. However, the question remained basically open as of a decade ago.

3.5 Is the metal-weak thick disk real?

Is there evidence for the additional presence of a metal-weak thick-disk (MWTD) population, rotationally supported, but extending to lower metallicity stars than the canonical thick disk?

Although the original suggestion that a MWTD thick-disk component may exist (Morrison, Flynn & Freeman 1990; Norris, Bessell & Pickles 1985) was supported by the analysis of Chiba & Beers (2000), claims to the contrary based on revised photometric studies (Twarog & Anthony-Twarog 1994) and high-resolution spectroscopic studies of suggested MWTD stars (e.g., Ryan & Lambert 1995) (but see also Bonifacio, Centurion & Molaro 1999) called the reality of the MWTD into question, at least at that time.

3.6 Are there stellar streams other than Sagittarius?

Can one identify other streams of stars, similar to the then-recognized Sgr stream, that might be associated with origin in stripped dwarf galaxies?

Helmi et al. (1999) presented the detection of a small number of halo stars that appeared as a statistically significant overdensity in an otherwise sparsely populated region of angular momentum phase space, and argued that they may have originated from the stripping of a once-coherent structure such as a dwarf galaxy. This inference was supported by additional data from Chiba & Beers (2000), and others since, but of course it was only one such example.

So, in toto, among the issues mentioned above, the data available as of a decade ago could at best claim only one clear “victory” (Issue 2), three strong “maybes” (Issues 1, 3, and 6), and two “yet to be decided” (Issues 4 and 5). Larger samples with well-understood selection biases were clearly needed.

4 WHAT DID WE LEARN DURING THE LAST DECADE?

Until recently, our global view of the Milky Way was hampered by the fact that most detected stars had no reliable distance estimates. Those stars that had usable distances were either limited to the solar neighborhood (e.g., for main-sequence stars in the Hipparcos sample to within ~ 100 pc, or only $\sim 1\%$ of our distance to the Galactic center), or to smaller pencil-beam surveys. Our knowledge of the basic structural components of the Milky Way was thus limited to indirect inferences based on stellar population models motivated by other spiral galaxies (e.g., Bahcall & Soneira 1980, Robin et al. 2003). This limitation was alleviated recently by the advent of SDSS, which provided accurate digital multi-band optical photometry across a quarter of the sky. The SDSS photometry enabled the development and application of photometric parallax methods, which in turn led to direct mapping of stellar distributions in the multi-dimensional space spanned by spatial coordinates, velocity components, and chemical abundance

measurements. The resulting maps provided the quantitative basis for separating the main structural components of the Galaxy, obtaining information on their phenomenological description, and enabled efficient searches for substructure and a robust comparison with various model predictions.

We first describe how these new data clearly reveal the disk and halo as two distinct Galaxy components, and then describe each of them in more detail. We do not discuss in detail here the third major Galaxy component, the bulge. For a recent excellent review of the bulge, see Minniti & Zoccali (2008). It is expected that spectroscopic data being collected by the SDSS-III Apache Point Observatory Galaxy Evolution Experiment (APOGEE) will soon yield unprecedented insight into chemical and kinematic properties of the bulge (Eisenstein et al. 2011, see also §8.1). We do not discuss the properties of the Galactic bar here, and refer the reader to recent studies by Cabrera-Lavers et al. (2008), Rattenbury et al. (2007), and Robin et al. (2011), which summarize the current state of the art and include relevant references.

4.1 Separation of the Main Structural Components

Before the disk and halo can be studied in detail, a robust and accurate scheme for classifying stars into these two components needs to be developed. Using photometric data for ~ 50 million stars, Jurić et al. (2008, hereafter Juric08) constructed 3-dimensional maps (data cubes) of the stellar number-density distribution for 19 narrow color bins that span spectral types from mid-F to early M-type stars. When the bin color is varied from the reddest to the bluest one, the maps are “zoomed out”, with subsamples covering distances ranging from 100 pc to 15 kpc. The distance to each star was estimated using a maximum likelihood

implementation of the photometric parallax method, and stars are binned and counted in small 3-dimensional pixels whose size depends on the dynamical range provided by each color bin and Poisson noise limits (typically there are 250,000 pixels per map). Examples of two-dimensional projections of the resulting maps are shown in Figure 3.

These maps are a powerful tool for studying the Milky Way’s stellar number density distribution. Traditional methods for modeling stellar counts in the magnitude-color space need to adopt a large number of poorly-known relations, such as the stellar initial mass function, stellar mass-luminosity relationship, stellar luminosity function, and a geometric description of the postulated components such as the disks, bulge, and halo. Alternatively, with these number-density maps the Milky Way’s structure can be examined without any a-priori assumptions about its components: The analysis of the Milky Way’s structure is then akin to studies of external galaxies.

The quantitative description of these maps is still a non-trivial task, due to the presence of rich substructures within the components. While halo substructure has been known for some time (Belokurov et al. 2006a, Ivezić et al. 2000, Majewski et al. 2003, Vivas & Zinn 2006, Yanny et al. 2000), these new maps demonstrate that disk substructure is also complex. Nevertheless, the gross behavior can be captured by assuming standard Galaxy models based on two exponential disks and a power-law halo. Jurić08 determined the best-fit parameter values for full two-dimensional smooth models, and further refined them using residual minimization algorithms (see Table 1).

A cross section of the maps from Figure 3 in the direction perpendicular to the disk plane is shown in Figure 4. The data shown in the middle and bottom panels

clearly confirm a change in the number-count behavior around $|Z| \sim 1\text{--}1.5$ kpc, interpreted as evidence for an extended “thick” disk component by Yoshii (1982) (who referred to it as a “halo” component, even though its inferred density was ten times that of the local halo and its scale height of ~ 2 kpc was commensurate with the values later determined by others) and Gilmore & Reid (1983). At the point where the additional, more-extended component becomes unable to explain the star counts, around $|Z| \sim 5$ kpc, another component – the stellar halo – is invoked to explain the data. Although these modern counts have exceedingly low statistical noise and fairly well-understood systematics, the three-component fit to the data shown in the bottom panel begs the question whether a single-component fit with some other function, parametrized with fewer free parameters, might suffice.

It turns out that the three additive components invoked to explain the counts exhibit distinctive chemical and kinematic behavior as well. Figure 5 shows a panoramic view of the variation in the median $[Fe/H]$ over an unprecedentedly large volume of the Galaxy. The map is based on photometric metallicity estimates for a sample of 2.5 million blue main-sequence stars (most of F spectral type) selected using very simple color and flux limits. It is easily discernible that the median metallicity farther than ~ 5 kpc from the Galactic plane is very uniform and about 1 dex lower than for stars within ~ 1 kpc from the plane.

The reason for the rapid decrease of median stellar metallicity with $|Z|$ for $|Z| < 5$ kpc, and very little variation farther from the plane, is illustrated in the left panel in Figure 6. The two distinct distributions imply different Galaxy components, the halo and the disk, and are clearly evident. High-metallicity disk stars dominate close to the plane, while low-metallicity halo stars dominate

beyond 3 kpc from the plane. The median metallicity for disk stars exhibit a vertical gradient, while the halo stars (at least in the relatively nearby volume) have a spatially invariant metallicity distribution. As $|Z|$ increases from $|Z| \sim 2$ kpc to $|Z| \sim 4$ kpc, halo stars become more numerous than disk stars, and the median metallicity drops by ~ 1.0 to 1.5 dex. A more detailed and quantitative discussion of these metallicity distributions can be found in Ivezić08.

These two components, with distinct metallicity distributions, also have vastly different kinematic behavior, as shown in the right panel in Figure 6. The high-metallicity disk stars exhibit large rotational velocity (about 220 km s^{-1}), while the low-metallicity halo stars display behavior consistent with no net rotation (to within $10\text{-}20 \text{ km s}^{-1}$). Similar to the behavior of their metallicity distributions, the rotational velocity for disk stars decreases with the distance from the Galactic plane, while it remains constant for nearby halo stars (see Figure 7).

Therefore, reasonably clean subsamples of halo and disk stars can be defined using a simple metallicity boundary $[Fe/H] = -1$. We proceed below with a more detailed discussions of each component.

5 THE MILKY WAY DISK

Recent massive datasets based on SDSS have confirmed, with exceedingly high statistical signal-to-noise ratios, the abrupt change of slope in the $\log(\text{counts})$ vs. $|Z|$ plot around $|Z| \sim 1$ kpc for disk stars (Juric08). This slope change was discovered almost three decades ago, and interpreted as evidence for two disk components: the thin disk and the thick disk. Over a similar range in $|Z|$, there are clearly detected vertical gradients in the median stellar metallicity and rotational velocity (Ivezić08, and references therein). A key question now

is whether the two disk components required to explain the counts can also be used to account for the chemical and kinematic measurements for the same stars. For example, are the metallicity and kinematic gradients due to the interplay of two additive components (with thick-disk stars dominating beyond $|Z| \sim 1$), or do they instead reveal a single disk with complex variations of basic properties (perhaps driven by a hidden variable, such as age)? In other words, do the new data require a disk decomposition into thin- and thick-disk components, and if so, what is an optimal way to define these components? It turns out that, even with the new data collected over the last decade, it is not easy to answer these questions.

The paper by Ivezić08 showed that the observed variations in the metallicity and velocity distributions of disk stars over the range $|Z| \sim 1 - 3$ kpc are only mildly inconsistent with the traditional simple decomposition into thin- and thick-disk components. However, they also found that the rotational velocity and metallicity at $|Z| \sim 1$ kpc, where the contributions of the two components are similar, are uncorrelated. This lack of correlation is in strong conflict with the traditional decomposition. Instead, Ivezić08 modeled the observed distributions using smooth shifts of the metallicity and velocity distributions that do not change their shape. They argued that their ability to describe the observations using functions with universal $|Z|$ -independent shapes has fundamental implications for disk origin – instead of two distinct components with different formation and evolution histories, the data could be interpreted with a single, albeit complex, disk.

On the other hand, Ivezić08 also pointed out that stars from the solar neighborhood, kinematically selected as thick-disk stars, have larger α -element abun-

dances, at the same $[Fe/H]$, than do thin-disk stars (e.g., Bensby et al. 2004; Fuhrmann 2004; Feltzing 2006; Reddy et al. 2006; Ramírez et al. 2007). In addition, the thick-disk stars, again selected kinematically, appear older than the thin-disk stars (e.g., Bensby et al. 2004; Fuhrmann 2004). Ivezić08 concluded that measurements of α -element abundances for samples of distant stars extending to several kpc from the midplane (as opposed to local samples) could resolve difficulties with traditional thin-thick disk decomposition when applied to their data. The means to obtain such a dataset was recently produced by Lee et al. (2011a), who showed that the $[\alpha/Fe]$ ratio can be estimated using the comparatively low-resolution SDSS spectra – for stars with temperatures in the range 4500 K to 7000 K and sufficient signal-to-noise, $[\alpha/Fe]$ estimates can be obtained with errors below 0.1 dex.

5.1 The Holy Grail for Thin-Thick Disk Decomposition: $[\alpha/Fe]$

Lee et al. (2011b, hereafter L11) analyzed a sample of $\sim 17,000$ G-type dwarfs with $[\alpha/Fe]$ measurements based on the techniques of Lee et al. (2011a). This dataset is the first massive sample of stars at distances of several kpc with reasonably accurate distance estimates, measurements of all three velocity components, measurements of both $[Fe/H]$ and $[\alpha/Fe]$, and selected using well-understood and simple color and flux selection criteria over a large area of sky. Thanks to these advantages, the L11 sample enabled a number of far-reaching observational breakthroughs:

1. The bimodal distribution of an unbiased sample of G-type dwarfs in the $[\alpha/Fe]$ vs. $[Fe/H]$ diagram (see Figure 8) strongly motivates the separation of the sample by a simple $[\alpha/Fe]$ cut into two subsamples that closely re-

semble traditional thin and thick disks in their spatial distributions, $[Fe/H]$ distributions, and distributions of their rotational velocity (see Figure 1 in L11).

2. The low- $[\alpha/Fe]$, thin-disk subsample has an $[Fe/H]$ distribution that does not strongly vary with position within the probed volume ($|Z| < 3$ kpc and $7 < R/\text{kpc} < 10$), with a median value of $[Fe/H] \sim -0.2$. Similarly, the metallicity distribution for the high- $[\alpha/Fe]$, thick-disk subsample has a median value of $[Fe/H] \sim -0.6$, without a strong spatial variation (see Figure 4 in L11).
3. The rotational velocity component, v_Φ , decreases linearly with distance from the midplane, $|Z|$, with a gradient of $d|v_\Phi|/d|Z| \sim -10 \text{ km s}^{-1} \text{ kpc}^{-1}$ for both the thin- and thick-disk subsamples (see Figure 8 in L11). The difference between the mean values of v_Φ for the two subsamples of $\sim 30 \text{ km s}^{-1}$ (asymmetric drift) is independent of $|Z|$, and explains the discrepancy between the $|Z|$ gradient of $-10 \text{ km s}^{-1} \text{ kpc}^{-1}$ reported by L11, and gradients about 2-3 times steeper reported for the full disk by earlier studies (e.g., Ivezić08, Casetti-Dinescu et al. 2011): as $|Z|$ increases from the midplane to 2-3 kpc, the fraction of thick-disk stars increases from $\sim 10\%$ to $>90\%$, and the observed gradient when all stars are considered is affected by both the intrinsic gradient for each component, and the velocity lag of thick-disk stars relative to thin-disk stars.
4. The rotational velocity component does not exhibit a gradient with respect to the radial coordinate, R , for thin-disk stars ($-0.1 \pm 0.6 \text{ km s}^{-1} \text{ kpc}^{-1}$; a “flat rotation curve”), and only a small and marginally detected gradient for thick-disk stars ($-5.6 \pm 1.1 \text{ km s}^{-1} \text{ kpc}^{-1}$).

5. The rotational velocity component and mean orbital radius are complex functions of the position in the $[\alpha/Fe]$ vs. $[Fe/H]$ diagram (see Figure 9). The rotational velocity component shows a linear dependence on metallicity for both the thin- and thick-disk $[\alpha/Fe]$ -selected subsamples (see Figure 11). The slopes of these v_Φ vs. $[Fe/H]$ correlations have opposite signs, $d|v_\Phi|/d[Fe/H] \sim -25 \text{ km s}^{-1}\text{dex}^{-1}$ for the thin disk, and $\sim 45 \text{ km s}^{-1}\text{dex}^{-1}$ for the thick disk, and do not strongly vary with distance from the midplane. These opposite gradients are partially responsible for the lack of correlation between v_Φ and $[Fe/H]$ at $|Z| \sim 1 \text{ kpc}$ reported by Ivezić08 (for the full sample; the other reason for the lack of correlation is systematic errors in the photometric metallicity estimator, see Appendix in L11).
6. Velocity dispersions for all three components of the local velocity ellipsoid increase with $[\alpha/Fe]$ as smooth functions, and continuously across the adopted thin/thick disk boundary (see Figure 10). Approximate values for the velocity dispersions $(\sigma_R, \sigma_Z, \sigma_\Phi)$ are $(40, 25, 25) \text{ km s}^{-1}$ for the thin-disk subsample and $(60, 40, 40) \text{ km s}^{-1}$ for the thick-disk subsample, respectively (not corrected for bias due to measurement errors; on average, about $10\text{-}15 \text{ km s}^{-1}$ should be subtracted in quadrature).
7. Orbital eccentricity distributions (model-dependent and determined using an analytic Stäckel-type gravitational potential from Chiba & Beers 2000) are significantly different for the two $[\alpha/Fe]$ -selected subsamples (see Figure 10 in L11), and exhibit strong variations with position and metallicity (see Figure 9 in L11). Notably, the shapes of the eccentricity distributions for the thin- and thick-disk populations are independent of distance from the plane, and include only a minute fraction of stars with eccentricity above

0.6.

The behavior of the $[\alpha/Fe]$ -selected subsamples of disk stars strongly argues in favor of the traditional decomposition into two (simpler) components. However, Lee et al. (2011b) did not explicitly test whether the counts of their two $[\alpha/Fe]$ -selected subsamples are consistent with the two best-fit additive exponential profiles obtained by Juric08, nor did they test in detail the hypothesis that the variation of the metallicity and rotational velocity distributions could be modeled using two simple components weighted by the counts ratio. We have used data from Lee et al. (2011b) (kindly provided by Young Sun Lee) to perform these tests here, as illustrated in Figure 12. We confirm that variations of the $[\alpha/Fe]$, $[Fe/H]$, and rotational velocity distributions with $|Z|$ can indeed be interpreted as due to the interplay of two simple components, whose relative strength variation with $|Z|$ is consistent with the Juric08 results. In particular:

- The $[\alpha/Fe]$ distribution in the fiducial bin $|Z|=400-600$ pc is bimodal. It can be explained as a linear combination of the slightly modified $[\alpha/Fe]$ distribution at $|Z|=2-3$ kpc (non-Gaussian, and presumably dominated by the thick disk) and a Gaussian distribution with a mean of $\langle[\alpha/Fe]\rangle = +0.11$ and rms of 0.06 dex, and with weights of 0.43 and 0.57, respectively (see the left panel in Figure 12). The only required modification of the $|Z|=2-3$ kpc $[\alpha/Fe]$ distribution is its shift towards lower $[\alpha/Fe]$ by 0.03 dex. The weights for the two components are consistent with a double-exponential fit to counts from Juric08, with the relative strength of the thick-disk component increased from Juric08's value of 0.13 to 0.16 here (a $\sim 2\sigma$ change).
- The $[Fe/H]$ distribution in the $|Z|=400-600$ pc bin can be explained as a

linear combination of the slightly modified $[Fe/H]$ distribution at $|Z|=2-3$ kpc (well described by a Gaussian) and a Gaussian distribution with a mean of $\langle [Fe/H] \rangle = -0.28$ and rms of 0.17 dex, and with the same weights as used for the $[\alpha/Fe]$ distribution (see the middle panel in Figure 12). The only required modification of the $|Z|=2-3$ kpc $[Fe/H]$ distribution is its shift towards higher $[Fe/H]$ by 0.2 dex (uncertain to within 0.05-0.1 dex).

- The rotational velocity distribution in the $|Z|=400-600$ pc bin can be explained as a linear combination of two Gaussian distributions (with $|v_\Phi|$ centered on 218 km s^{-1} and 190 km s^{-1} , and with velocity dispersions of 22 km s^{-1} and 40 km s^{-1} , respectively), again with the same weights as used for the $[\alpha/Fe]$ and $[Fe/H]$ distributions (see the right panel in Figure 12). When corrected for velocity measurement errors (dominated by proper-motion errors), these dispersions become 16 km s^{-1} and 38 km s^{-1} , respectively.

The fact that all three distributions ($[\alpha/Fe]$, $[Fe/H]$, and v_Φ) in the $|Z|=400-600$ pc bin can be described as linear combinations of the corresponding distributions in a distant bin dominated by the thick-disk component and a best-fit thin-disk Gaussian, with the same weights for all three cases that are consistent with the double-exponential fit to the star counts, strongly supports the hypothesis that the Milky Way disk comprises at least two distinct components⁷. The

⁷Our analysis cannot exclude the possibility that the disk structure is more complex than implied by the sum of only two simple components. Indeed, Figure 10 shows that all three velocity dispersions are smooth functions of the $[\alpha/Fe]$ ratio (and not step functions, for example). This smoothness implies that an $[\alpha/Fe]$ -based disk decomposition into only two components is at best a very good approximation, but definitely not the whole story. Most recently (after this review was submitted), Bovy, Rix & Hogg (2011) re-analyzed the same dataset and concluded

required shifts of $[\alpha/Fe]$ and $[Fe/H]$ distributions between the two Z bins imply vertical gradients of ~ 0.015 dex kpc^{-1} and ~ 0.1 dex kpc^{-1} for the thick-disk component (both with a relative uncertainty of about 30%). Together with the rotational velocity gradient of ~ 10 $\text{km s}^{-1} \text{kpc}^{-1}$ (for both the thin- and thick-disk components) from Lee et al. (2011b), these vertical gradients represent strong constraints on models for thick-disk formation.

We note that, out of six distributions (three quantities for the two adopted disk components), the only strongly non-Gaussian distribution is the thick-disk $[\alpha/Fe]$ distribution, that is, the $[\alpha/Fe]$ distribution for stars in the $|Z|=2-3$ kpc bin (dashed line in the left panel of Figure 12). Its skewness is due to the presence of about 15% of the stars with $[\alpha/Fe] < +0.2$; their existence is puzzling. According to Lee et al. (2011b) and our own analysis of the kinematic and metallicity behavior of stars with $[\alpha/Fe] < +0.2$, they represent the thin-disk component. For example, in the $|Z|=400-600$ pc bin there are no stars with $[\alpha/Fe] < +0.2$ that also have $[Fe/H] < -0.5$ or $|v_\Phi| < 140$ km s^{-1} , and stars with $[Fe/H] < -0.5$ and $|v_\Phi| < 140$ km s^{-1} have a median $[\alpha/Fe]$ of +0.40, with an rms of only 0.05 dex. However, the puzzle is that, according to the double-exponential fit to star counts, the $|Z|=2-3$ kpc bin should contain only $\sim 1\%$ of thin-disk stars, not 15%. In addition, for stars with $|Z|=2-3$ kpc, the subsample with $[\alpha/Fe] < +0.2$ has the same $[Fe/H]$ and v_Φ distributions as the subsample with $[\alpha/Fe] > +0.2$. Hence, it may be that the skewed $[\alpha/Fe]$ distribution for stars in the $|Z|=2-3$ kpc bin simply reflects a non-Gaussian measurement error that evidence for the bimodal distribution of $[\alpha/Fe]$ all but disappears when selection effects are accounted for. The implication of their result is that a continuous distribution of scale heights is a more appropriate model than a simple two-component model for describing SDSS data from

distribution for the method described in Lee et al. (2011a). It is noteworthy that stars from the $|Z|=2-3$ kpc bin are on average about 3 mags fainter than stars from the $|Z|=400-600$ pc bin ($r \sim 18$ vs. $r \sim 15$). Needless to say, independent measurements of $[\alpha/Fe]$ for stars with $Z=2-3$ kpc would provide valuable clues as to the proper interpretation.

In summary, when disk stars are separated by a simple, well-motivated $[\alpha/Fe]$ cut, the resulting subsamples display remarkably simple spatial, kinematic, and metallicity distributions, consistent with the traditional decomposition into thin- and thick-disk components. It is likely that the differences in $[\alpha/Fe]$ reflect different star-formation timescales (enrichment by Type Ia vs. Type II supernovae for low and high $[\alpha/Fe]$ values over long and short timescales, respectively; see Bensby, Feltzing & Lundström (2004); Johnston et al. (2008)). Therefore, after detailed analysis of full 7-D phase space, SDSS data finally confirm that $[\alpha/Fe]$ measurements provide the most robust decomposition of disk stars into thin-disk and thick-disk components.

On the other hand, a few words of caution are due here. The main results from L11 still need to be confirmed by independent datasets. It is somewhat worrisome that the RAVE-based results from Burnett et al. (2011) for the disk $[Fe/H]$ distribution differ from the L11 results. At $|Z| \sim 0$, the RAVE results are about 0.2 dex more metal rich (although we note that the SDSS result for the median $[Fe/H] = -0.2$ at $|Z| = 0$ is consistent with the results from Nordström et al. 2004), and the discrepancy increases to ~ 0.3 dex at $|Z| \sim 2.5$ kpc. It is not clear yet whether the discrepant results reported by the RAVE and SDSS surveys arise from differences in their adopted metallicity scales, or are due to unaccounted selection effects in the RAVE analysis (see Section 6 in

Burnett et al. 2011). Encouragingly, the spatial metallicity gradients at $|Z| \sim 1$ kpc, where thick-disk stars become more numerous than thin-disk stars, are robustly detected and similar in both studies, $d[Fe/H]/d|Z| \sim -0.2$ dex kpc^{-1} (for stars from both components considered together). The median $[Fe/H]$ at $|Z| \sim 1$ kpc reported by Lee et al. (2011b) is -0.5 dex, about 0.2 dex lower than reported by Burnett et al. (2011) using RAVE, and about 0.2 dex higher than reported by Ivezić08 using photometric metallicities from the SDSS imaging survey. It remains to be seen how the $[\alpha/Fe]$ measurements from the SDSS and RAVE surveys compare to each other; further study will presumably provide illumination.

The Burnett et al. (2011) study also reports age determination for RAVE stars (based on stellar models), with typical uncertainties of about a factor of two (see their Figure 7). They detect a remarkable age gradient between the Galactic midplane and $|Z| \sim 2$ kpc (see their Figures 16 and 17), which is at least qualitatively consistent with the variation of the $g - r$ color of turnoff stars seen by SDSS, and the velocity dispersion-age correlations for local disk stars from Nordström et al. (2004), Rocha-Pinto et al. (2004a), and West et al. (2008). They also detect a complex variation of metallicity distribution with stellar age (see their Figure 18). In particular, the oldest stars ($> 8 - 9$ Gyr) are predominantly low-metallicity ($[Fe/H] < -0.5$). These age data represent a valuable addition to the L11 results. Nevertheless, determining age for individual stars is exceedingly difficult (Pont & Eyer 2004, Soderblom 2010) and one needs to consider all the caveats discussed by Burnett et al. at the end of their Section 7. Given these difficulties, it seems best to proceed with caution. There would be clear advantage in, at the very least, obtaining age estimates for the SDSS sample (using

different methodologies than used for the RAVE data), and making a more direct comparison based on this information.

Last but not least, we note that the observational material for studying the bulge of the Milky Way has also significantly improved during the last decade. Clarkson et al. (2008) used HST to detect proper motions for over 15,000 bulge stars and “dissected” the kinematic properties of the bulge as a function of distance along the line of sight. A radial-velocity survey of bulge stars (BRAVA; Rich 2011) obtained data for 10,000 red giants in the Southern Galactic bulge, and found clear departures from solid-body rotation that are consistent with an edge-on bar. Rangwala & Williams (2009) and Rangwala, Williams & Stanek (2009) reported radial-velocity and metallicity measurements for over 3,000 bulge stars, and now even $[\alpha/Fe]$ measurements are available for large samples of stars. For example, Gonzalez et al. (2011) determined $[\alpha/Fe]$ for 650 red-giant stars using $R \sim 22000$ spectroscopy, and found support for two bulge components in the observed metallicity and $[\alpha/Fe]$ distributions, reminiscent of the disk separation into thin- and thick-disk components. They argue that the chemical similarity of the low-metallicity bulge component and the thick disk hints for rapid, early formation for both structures. It is likely that such observational progress will lead to additional studies that simultaneously consider all of the major structural components of the Galaxy.

5.2 Comparisons of Observations with Disk Formation Models

Despite the past three decades of thick-disk studies, there is still no consensus on models for its formation and evolution (the thick disk is not unique to the Milky Way; for a review of thick disks in other galaxies, see van der Kruit & Freeman 2011).

The proposed scenarios can be broadly divided into two groups: violent origin, such as heating of an existing thin disk due to mergers, and secular evolution, such as heating due to scattering off molecular clouds and spiral arms (see L11 for a detailed discussion and references). In the first set of scenarios, the fraction of thick-disk stars accreted from merged galaxies remains an important and still unconstrained parameter, and further complexity arises from the possibility that some stars may have formed in situ, when star formation is triggered in mergers of gas-rich galaxies (Brook et al. 2007, and references therein). In the second set of scenarios, the main modeling difficulty is the lack of detailed knowledge about the relative importance of various scattering mechanisms. Over the last decade, the radial-migration mechanism (Sellwood & Binney 2002; Roškar et al. 2008b; Schönrich & Binney 2009b; Minchev & Famaey 2010) has been developed as an attractive secular scenario. Due to various computational and other difficulties, numerical models that combine the main features of the violent and secular scenarios are few.

The recent observational material contains rich information for model testing, and is beginning to rule out some models. Modern data include simultaneous measurements of many observables for large numbers of stars, and enable qualitatively new approaches to tests of disk-formation models. The more observables that are measured, the more powerful these tests become, because the data can be “sliced” along multiple axes in a variety of ways while maintaining small statistical errors due to the large sample sizes. For example, the two eccentricity distributions for $[\alpha/Fe]$ -selected subsamples are much more powerful model discriminators than the eccentricity distribution for all stars lumped together. On the other hand, the complexity of such tests can be formidable – even a minimal-

istic selection of observables, such as coordinates R and $|Z|$, chemical parameters $[Fe/H]$ and $[\alpha/Fe]$, and the essential kinematic parameters, rotational velocity and orbital eccentricity, span a six-dimensional space. The basic model vs. data comparisons for testing thick-disk formation and evolution scenarios include:

1. Comparison of the observed distribution of stars in the $[\alpha/Fe]$ vs. $[Fe/H]$ diagram, as a function of the position in the Galaxy (e.g., Can models reproduce the bimodal distribution seen in Figure 8? Does the fraction of the sample in the high- $[\alpha/Fe]$ component increase with the distance from the midplane as observed?).
2. For subsamples defined using $[\alpha/Fe]$, comparison of the shapes of their metallicity and kinematic distributions (e.g., Can models reproduce the $[Fe/H]$ distributions seen in Figure 4 from L11 and in Figure 12, or the eccentricity distributions seen in their Figure 10?).
3. For subsamples defined using $[\alpha/Fe]$, comparison of the variations of their number density and low-order statistics for metallicity and kinematic distributions (e.g., $\langle v_\Phi \rangle$, velocity dispersions, mean/mode/median eccentricity) with position in the Galaxy (e.g., Can models reproduce the spatial gradients of the $\langle v_\Phi \rangle$ seen in Figure 8 from L11, or the spatial gradients of the mean eccentricity from their Figure 9?).
4. Comparison of high-order correlations between the observables, such as the complex variation of the mean rotational velocity with position in the $[\alpha/Fe]$ vs. $[Fe/H]$ diagram (see Figures 9 and 11), or the variation of the orbital eccentricity with metallicity (see Figure 9 in L11).

A few of the above tests have already been performed. In a strict statistical

sense, all the proposed models can be outright rejected because the observed distributions of various parameters have very low statistical noise, and the models are not sufficiently fine tuned (yet) to reproduce them (e.g., none of model eccentricity distributions comes even close to passing the Kolmogorov-Smirnov test). For this reason, most of the model vs. data comparisons are still qualitative, and only gross inconsistencies can be used to reject certain scenarios.

Beginning with Sales et al. (2009), a number of recent papers have used the shape of the derived orbital eccentricity distribution as a means to compare models to data from the SDSS and RAVE surveys (Casetti-Dinescu et al. 2011, Di Matteo et al. 2011, Dierickx et al. 2010, Lee et al. 2011b, Loebman et al. 2011, Wilson et al. 2011). We note that orbital eccentricity is derived from observations in a model-dependent way (a gravitational potential must be assumed), and different assumptions may lead to systematic differences between the observed and predicted distributions. Another detail to keep in mind is that stars with small rotational velocities are often excluded to minimize the contamination of disk samples by halo stars. However, disk stars with very high orbital eccentricity are also excluded by the same cut, and their exclusion may lead to unjustified model rejection. Although there are detailed differences in the eccentricity distributions derived from data, the mode of the distributions for stars at about 1-2 kpc from the midplane is typically in the range 0.2–0.3, and the fraction of stars with eccentricities larger than 0.8 are below a percent or so (unfortunately, none of recent papers listed above show cumulative distributions, nor directly compare with various data-based distributions).

In most of the recent studies, four published simulations of thick disks formed by (a) accretion from disrupted satellites, (b) heating of a pre-existing thin disk

by a minor merger, (c) radial migration and (d) gas-rich mergers (see Sales et al. for references), are confronted with data. The model predictions for eccentricity distributions are nicely summarized in Figure 3 from Wilson et al. (2011) and Figure 17 from Casetti-Dinescu et al. (2011). Scenario (a) produces an eccentricity distribution with a mode at ~ 0.5 , and scenario (b) predicts a bimodal eccentricity distribution that includes too many stars ($\sim 10\%$) with eccentricities above 0.8 (see Figure 3 in Sales et al. and Figure 10 in L11, but note that stars with eccentricity larger than 0.8 exist in the sample from Casetti-Dinescu et al. 2011). In addition, scenario (b) does not exhibit the characteristic change of slope in the $\log(\text{counts})$ vs. $|Z|$ plot (see Figure 1 in Sales et al.). These discrepancies are the main reasons for the growing consensus that the gas-rich mergers and radial-migration scenarios are in best agreement (more precisely, least disagreement) with the present data.

Loebman et al. (2011) performed a number of the data vs. model tests listed above, in the limited context of the radial-migration models developed by Roškar et al. (2008). They demonstrated that the overall features seen in the SDSS data, such as the gradients of metallicity and rotational velocity with distance from the midplane (see Figure 13), as well as the gradients of rotational velocity with metallicity (see their Figure 15), and the complex structure seen for the mean rotational velocity in the $[\alpha/Fe]$ vs. $[Fe/H]$ diagram (their Figure 14), are qualitatively reproduced by the models (at a detailed quantitative level there is room for improvement). We note an important implication of those models – $[\alpha/Fe]$ should be an excellent proxy for age. Using a different numerical implementation of the radial-migration scenario, Schönrich & Binney (2009a) and Schoenrich (2011), Schönrich & Binney (2009b) demonstrated good agreement with the local solar

neighborhood data from the Geneva-Copenhagen survey (Nordström et al. 2004).

These model successes hint that the thick disk may be a ubiquitous Galactic feature generated by stellar migration (though note that a similar analysis has not yet been carried out with the gas-rich merger models). However, although these models at least qualitatively reproduce much of the complex behavior seen in the data, radial migration cannot be the full story – there exist counter-rotating disks observed in some galaxies (Yoachim & Dalcanton 2008), thick disks are less prominent in high-mass galaxies (Yoachim & Dalcanton 2006), and remnants of merged galaxies are directly observed in the Milky Way (see the right column in Figure 3 and the discussion in §6.4 below).

5.3 A Summary of Recent Disk Studies

To summarize, given the new SDSS, RAVE, and other data, there is no doubt that the spatial and kinematic behavior of disk stars greatly varies as a function of their chemical composition, parametrized by the position in the $[\alpha/Fe]$ and $[Fe/H]$ diagram. While quantitative details still differ somewhat between different analysis methods, and between the SDSS and RAVE datasets, robust conclusions are that the high- $[\alpha/Fe]$ subsample has all the characteristics traditionally assigned to the thick disk: larger scale height, lower $[Fe/H]$, a rotational velocity lag, and larger dispersions for all three velocity components, when compared to the low- $[\alpha/Fe]$ subsample. There is mounting evidence that the ages of these stars are higher than those in the low- $[\alpha/Fe]$ subsample, and similar to the age of Galaxy, although the interpretation of age data is much more prone to systematics than chemical and kinematic data.

Despite this tremendous observational progress, there is still no consensus on theories for the origin of thick disk. The two main contenders remain gas-rich mergers and radial-migration scenarios, while the accretion and disk heating scenarios appear to be in conflict with the data. Nevertheless, no generic model/scenario should be fully rejected yet, since detailed comparisons with data have only begun and the input model parameter space has not been fully explored. Assuming that SDSS measurements reported in L11 survive further scrutiny (e.g., when compared to RAVE and other datasets), modelers will be kept busy for some time trying to explain the rich observational material collected over the last few years.

6 THE MILKY WAY HALO

Studies of the Galactic halo provide unique insights on the formation history of the Milky Way, and for the galaxy formation process in general, because dynamical timescales are much longer than for disk stars and thus the “memory of past events lasts longer” (e.g., Johnston, Hernquist & Bolte 1996; Mayer et al. 2002). The last decade has seen tremendous progress in both observations and simulations of the Milky Way halo. For example, Wetterer & McGraw (1996) pointed out that there were only nine RR Lyrae stars discovered at Galactocentric distances larger than 30 kpc at that time. With the advent of SDSS, 2MASS, QUEST, and other surveys, there are now many hundreds of RR Lyrae stars (Sesar et al. 2010a, Vivas & Zinn 2006) and thousands of BHB stars (Brown et al. 2010, Sirko et al. 2004, Xue et al. 2008) detected all the way to ~ 100 kpc. The 2MASS point source catalog has provided an all-sky view of the distribution of M giants beyond 30 kpc (Majewski et al. 2003), and a large sample of carbon-rich giants

have been observed at similar distances (Ibata et al. 2001b). With SDSS data, it is now possible to study the halo within ~ 10 -20 kpc using tens of millions of main-sequence stars (Bell et al. 2008, Belokurov et al. 2007b, Newberg et al. 2007, 2002, Juric08, Ivezić08, Bond10). Concurrently, models for the formation and evolution of stellar halos have grown increasingly more sophisticated and predictive (Bullock et al. 2001; Bullock & Johnston 2005; Font et al. 2011; Ghigna et al. 2000; Helmi 2008; Johnston et al. 2008; Law, Johnston & Majewski 2005; Springel et al. 2008; Starkenburg et al. 2009). For example, contemporary simulations of galaxy formation predict that stellar halos of Milky Way-type galaxies are assembled from inside out, with the majority of the mass (50%-80%) coming from several massive (10^8 - $10^{10} M_{\odot}$) satellites that have merged more than 9 Gyr ago, while the remaining mass comes from lower mass satellites accreted in the past 5-9 Gyr (Bullock & Johnston 2005, De Lucia & Helmi 2008, Font et al. 2011).

The new data collected over the last decade led to significantly improved quantitative understanding of the spatial distribution, kinematics, and metallicity distribution of halo stars. We first review results for the relatively nearby halo within ~ 20 kpc, probed in situ⁸ with main-sequence stars, then summarize observations out to ~ 100 kpc with various other more luminous tracers, and finish with a discussion of stellar streams and other halo substructures.

⁸Hereafter we use *in situ* to refer to measurements of stars located where their stellar population dominates, as opposed to “extrapolated properties” based on local samples.

6.1 The Smooth Halo Behavior as Probed by Main-Sequence Stars

Despite the presence of abundant halo substructure (see below), it is possible to describe the distribution of halo stars within $R \sim 20$ kpc at an impressive level of fidelity using a simple smooth, oblate, and cylindrically symmetric power-law model. The Juric08 study used SDSS data for ~ 50 million stars, together with a photometric parallax method, to estimate their distances (see §1.3.1), and found that the local stellar halo can be modeled as

$$n(R, Z) = n_o f_H \left(\frac{R_\odot^2}{R^2 + (Z/q_H)^2} \right)^{\frac{n}{2}}, \quad (1)$$

where $n(R, Z)$ is the number of stars per unit volume (“number density”), as a function of the cylindrical coordinates R and Z , n_o is the local (at the solar position) number density of all stars, f_H is the local fraction of halo stars, and q_H parametrizes deviations from spherical symmetry ($q_H < 1$ for an oblate halo). After masking regions with obvious localized overdensities, Juric08 obtained the following best-fit parameters: $f_H = 0.005$, $q_H = 0.64$, and $n = 2.8$. Examples of the observed $n(R, Z)$, the best-fit model, and the fit residuals from the Juric08 study are shown in Figure 3 (note that the disk component is also shown; see also the bottom panel in Figure 4). It is important to remember that the dataset used by Juric08 does not extend beyond $R \sim 20$ kpc and $|Z| \sim 10$ kpc. Indeed, additional data suggest that the Juric08 single power-law halo cannot be extrapolated beyond 20 kpc (see below).

Recently, Bonaca et al. (2012) examined whether eq. 1 is an appropriate model for the distribution of main-sequence turn-off halo stars observed by the Eight Data Release of the SDSS (DR8, Aihara et al. 2011). DR8 covers almost a fac-

tor of two more area than analyzed by Juric08, including an order of magnitude greater coverage of the Southern Galactic hemisphere. After accounting for known overdensities and streams (Virgo, Hercules-Aquillae, Sagittarius; see § 6.4), Bonaca et al. (2012, to be submitted) find no evidence for any residual triaxiality of the stellar halo. To the extent that can be probed with SDSS imaging data, the halo within 10-20 kpc from the Galactic center remains well described by an oblate ellipsoid (for a discussion of more distant parts of the halo, see § 6.2).

Although the SDSS spectroscopic survey has provided metallicity measurements for a large number of stars, spectroscopic estimates of $[Fe/H]$ are available for $< 1\%$ of the stars used by Juric08. To provide a panoramic map of the $[Fe/H]$ distribution for halo stars, Ivezić08 utilized a photometric metallicity method (see §1.3.2). Their $[Fe/H]$ map, shown in Figure 5, demonstrates that the median metallicity of halo stars is essentially invariant within the probed volume; Ivezić08 determined an upper limit for its spatial gradient of $0.005 \text{ dex kpc}^{-1}$ within $|Z| < 10 \text{ kpc}$. The local halo $[Fe/H]$ distribution is well described by a Gaussian centered on $[Fe/H] = -1.46$, with an rms of 0.30 dex .

In the third paper of the Milky Way tomography series, Bond10 used the large database of SDSS-POSS proper motions (see §2.2), and radial-velocity measurements from the SDSS spectroscopic survey (see §2.1), to quantify the kinematic behavior of halo stars. Similarly to the behavior of counts and metallicity, Bond10 found that halo kinematics also admit a simple model description. The very complex behavior of measured proper motions (see Figure 14) and radial velocities (see Figure 15) on the sky can be explained with a simple triaxial velocity ellipsoid that is invariant in spherical coordinates, with $\sigma_r=141 \text{ km s}^{-1}$, $\sigma_\Phi=85 \text{ km s}^{-1}$, $\sigma_\theta=75 \text{ km s}^{-1}$, and their uncertainties of $\sim 5 \text{ km s}^{-1}$. For example, the

substantial variation in the dispersion of measured radial velocities across the sky seen in the bottom left panel in Figure 15 is due to the change of the orientation of velocity ellipsoid with respect to the line of sight (see Figure 16), rather than some localized substructure. A similar triaxial velocity ellipsoid was measured by Smith et al. (2009), using more robust proper motions based on only SDSS astrometry (as opposed to the SDSS-POSS dataset used by Bond10), although in only a single direction on the sky. This remarkable alignment of the halo velocity ellipsoid with spherical coordinates (halo stars “know” where the Galactic center is – see Figure 16!) is also supported by independent data from the RAVE survey (Siebert et al. 2008), and represents a strong constraint on the shape of gravitational potential – the potential must be close to spherically symmetric within ~ 20 kpc from the Galactic center (Smith, Wyn Evans & An 2009, and references therein). The spherical symmetry of the gravitational potential is also invoked as an explanation for the lack of precession of the orbital plane of debris of the Sagittarius dwarf spheroidal (see below) by Fellhauer et al. (2006), which is implied if the observed bifurcation in the distribution of debris is due to multiple (young and old) streams. On the other hand, Helmi (2004) concluded that the dark matter halo has a prolate shape, based on modeling the dynamics of the leading (old) stream.

It is noteworthy that the difference of 10 km s^{-1} between σ_{Φ} and σ_{θ} measured by Bond10 is only marginally detected (less than 2σ significance if the measurement errors are $\sim 5 \text{ km s}^{-1}$, as claimed by Bond10). An even smaller difference was measured by Smith et al. (2009), using proper motions based on only SDSS astrometry ($\sigma_{\Phi}=82 \text{ km s}^{-1}$ and $\sigma_{\theta}=77 \text{ km s}^{-1}$), with quoted errors of $\sim 2 \text{ km s}^{-1}$ (which are likely to be underestimated because distance errors

are not taken into account; both Bond10 and Smith et al. used the photometric parallax relation from Ivezić08). The significance of the difference between σ_Φ and σ_θ is important, because if $\sigma_\Phi = \sigma_\theta$, then the halo stellar density distribution should not be oblate, as measured by Juric08, but spherical instead (Smith, Wyn Evans & An 2009). Indeed, using kinematic constraints based on their measurements of σ_Φ and σ_θ , Smith et al. (2009) obtained an implied stellar halo flattening parameter of $q_H = 0.98$, in puzzling disagreement with the value of $q_H = 0.64$ measured in situ by Juric08. Nevertheless, Smith et al. pointed out that their solution for the stellar halo density distribution is not unique, thus the resolution of this puzzle may be in multi-component models, such as those discussed below.

Finally, we point out that although the model advocated by Bond10 assumes no halo rotation, their data could not rule out net rotation at the level of up to ~ 20 km s⁻¹. The key systematic errors limiting the precision are the distance scale errors, uncertain correction to the local standard of rest, and systematic errors in radial-velocity and proper-motion measurements (see their Section 5.3). Nevertheless, Smith et al. (2009) did not detect halo rotation from their sample with more robust proper-motion measurements; similarly Allende Prieto et al. (2006) found no evidence for halo rotation using SDSS radial velocities.

6.2 Beyond a Simple Power Law: One Halo, Two Halos, Many Halos?

Due to the SDSS faint flux limit, the Juric08 results for the spatial distribution of main-sequence halo stars are limited to the volume within $R \sim 20$ kpc and $|Z| \sim 10$ kpc. Additional data suggest that the Juric08 single power-law halo

model cannot be extrapolated beyond these limits. First, a kinematic analysis of halo stars, within the same distance limits by Carollo et al. (2010, 2007), suggests that the halo consists of two broadly overlapping structural components, an “inner halo” and an “outer halo” (see Figure 17). These labels are not merely descriptors for the regions studied, but rather are labels for two individual stellar populations. These components exhibit different spatial density profiles, stellar orbits, and stellar metallicities, with the inner halo to outer halo transition occurring, according to these authors, at Galactocentric distances of 15-20 kpc. This result follows from their kinematic analysis of SDSS calibration stars within 4 kpc (including stars other than main-sequence dwarfs), and is not an in situ measurement. The inner halo was shown to comprise a population of stars exhibiting a flattened spatial density distribution, with an inferred axial ratio on the order of $q_H \sim 0.6$ and $n = 3.2 \pm 0.2$, no rotation at the level of $\sim 10 \text{ km s}^{-1}$, and a metallicity distribution peaked at $[Fe/H] \sim -1.6$. These properties of the inner halo are in very good agreement with the results from Jurić08, Ivezić08, and Bond10, based on direct mapping (as opposed to indirect inferences in the Carollo et al. analysis). The outer halo comprises stars that exhibit a more spherical spatial density distribution, with an axial ratio $q_H \sim 0.9$ and $n = 1.8 \pm 0.3$, a clear retrograde net rotation ($\langle v_\Phi \rangle \sim -80 \text{ km s}^{-1}$), and a metallicity distribution peaked at $[Fe/H] \sim -2.2$.

The Carollo et al. results were recently questioned by Schönrich, Asplund & Casagrande (who argued that distance errors resulting from luminosity biases, and/or improper accounting for measurement errors and the use of Gaussian fitting resulted in a distorted identification of the halo components. They re-evaluated the same data and failed to detect “any reliable evidence for a counter-rotating

halo component.” In a rebuttal of these claims, Beers et al. (2011) re-analyzed their original dataset (re-classifying the main-sequence turnoff stars that were the primary source of concern for Schönrich et al.), pointed out that Schönrich et al. had themselves adopted an incorrect main-sequence luminosity relationship from Ivezić08 (which significantly affected their interpretation), and confirmed the presence of a lower metallicity counter-rotating halo (whether or not the turnoff stars in question were used in the analysis). The Beers et al. paper also provided additional evidence for the presence of an inner/outer halo dichotomy, based on other datasets and methods of analysis. They concluded that “Ultimately, geometric distances from Gaia for stars in the halo populations will eliminate any remaining questions concerning the impact of uncertain photometric parallaxes on these conclusions. However, our view is that presently available data already reject the single-halo interpretation beyond reasonable doubt.”

Ideally, to resolve these ambiguities the spatial distribution of halo stars, and their kinematic and chemical behavior, should be measured in situ using main-sequence stars. Unfortunately, even turnoff stars with $M_r = 5$ would be as faint as $r = 25$ at a distance of 100 kpc. Until the advent of LSST and Gaia (for robust calibration of the photometric parallax relation) surveys (see §8), it will not be possible to perform such measurements over a large area of sky. Nevertheless, several studies over small sky areas, or using tracers more luminous (but less numerous!) than main-sequence stars, have provided further, and often intriguing, insights into the properties of the halo.

The analysis of de Jong et al. (2010), based on a color-magnitude diagram fitting approach using templates of old stellar populations with differing metallicities, produced a sparse three-dimensional map of the stellar distribution of

SDSS main-sequence turnoff stars within $r \sim 30$ kpc, derived from the ten “vertical” (in Galactic coordinates) photometric scans of width 2.5° obtained during the SEGUE sub-survey of SDSS-II. Their Figure 6 provides clear in situ evidence for a shift in the mean metallicity of the Milky Way’s stellar halo – within $r \sim 15$ kpc their derived stellar halo exhibits a mean metallicity of $\langle [Fe/H] \rangle \sim -1.6$, changing to $\langle [Fe/H] \rangle \sim -2.2$ at larger Galactocentric distances. In addition, inspection of the spatial density profiles of their template populations (their Figure 7) suggests rather different spatial behaviors for their “inner-halo like” template population and that of their “outer-halo like” template population. Their derived inner-halo density profile falls off rapidly with distance from the Galactic center to $r \sim 15 - 20$ kpc; beyond this region a substantially lower density, slowly varying, outer-halo density profile was found. Note that the de Jong et al. analysis was restricted to distances $r < 30$ kpc. When a single power-law was fit to this entire region they obtained an index of $n = 2.75 \pm 0.07$, in excellent agreement with the previous work of Bell et al. (2008) and Juric08.

Over most of the sky observed by SDSS, the distribution of blue main-sequence stars can be mapped out to a distance limit of $\sim 20-30$ kpc. However, in about ~ 300 deg² of sky from the so-called Stripe 82 area, co-added imaging based on multiple observations has a limiting magnitude about two mags fainter ($r \sim 24$) than single-epoch SDSS data, and can be used to map the number-density distribution of blue main-sequence stars out to ~ 40 kpc. Sesar et al. (2010a) analyzed this dataset and found that it agrees well with the extrapolations of the Juric08 model to Galactocentric distances less than ~ 25 kpc. However, at larger distances the model overpredicts the observed counts by about a factor of two, strongly suggesting that the halo stellar number-density profile becomes much

steeper. Although Sesar et al. could not derive precise quantitative adjustments to the Juric08 model parameters, they approximately estimated a change of the halo power-law index from $n \sim 3$ to about $n \sim 5$. They also detected a decrease in the median metallicity between Galactocentric radii of 10 kpc and 20 kpc of $0.02 \text{ dex kpc}^{-1}$, a factor of four larger than the upper limit of $0.005 \text{ dex kpc}^{-1}$ determined by Ivezić08 within 10 kpc. Extrapolation of this gradient to a Galactocentric radius of ~ 50 kpc would result in a metallicity value similar to that determined for the outer halo by Carollo et al. Note that, in the interpretation of Carollo et al., this “gradient” is actually the result of the lessening degree of importance of the inner halo, relative to the more metal-poor outer halo, as one moves outward. Once the outer-halo population dominates, there is no expected decline in metallicity.

Sesar, Jurić & Ivezić (2011) used the Canada-France-Hawaii Telescope Legacy Survey (CFHTLS) data, covering 170 deg^2 , to study the distribution of near-turnoff main-sequence stars along four lines of sight to heliocentric distances of ~ 35 kpc. They found that the halo stellar number-density profile becomes steeper at Galactocentric distances greater than ~ 28 kpc, with the power-law index changing from $n = 2.62 \pm 0.04$ to $n = 3.8 \pm 0.1$. They measured the oblateness of the halo to be $q_H = 0.70 \pm 0.01$ (statistical error only) and detected no evidence of it changing across the range of probed distances, nor any changes in the median metallicity.

Deason, Belokurov & Evans (2011) explored similar issues, using a sample of $\sim 20,000$ BHB and blue straggler stars detected by SDSS over $14,000 \text{ deg}^2$ of sky, and obtained almost identical results to those from Sesar, Jurić & Ivezić (2011), based on main-sequence stars. Their best fitting model has an inner power-law

index of $n = 2.3$ and an outer index of $n = 4.6$, with the transition occurring at ~ 27 kpc, and a constant halo flattening of $q_H = 0.6$. They concluded that “the stellar halo is composed of a smooth underlying density, together with some additional substructures such as the Virgo Overdensity and the Sagittarius Stream”. In addition, the distribution of RR Lyrae stars from the SEKBO survey (Keller et al. 2008), and of RR Lyrae stars from SDSS Stripe 82 data (Sesar et al. 2010a, Watkins et al. 2009), indicates a steeper density profile beyond 30 kpc. Furthermore, using the LONEOS sample of RR Lyrae stars, Miceli et al. (2008) argued for the presence of a dual halo in order to account for the apparently very different spatial profiles of Oosterhoff Type I and Oosterhoff Type II subsamples. Taken together, these studies provide strong in situ support for rejecting the single-halo hypothesis.

6.3 What is the Nature of the Outer Halo?

Despite the growing evidence that stellar distribution in the Milky Way halo is more complex than a smooth single power law, and may well comprise at least two primary stellar populations, quantitative knowledge about the most distant parts of the Milky Way is still limited. The smooth analytic descriptions of the stellar distribution discussed above begin to fail beyond 30 kpc from the Galactic center due to the presence of rich substructure, as discussed in the next section. Even when these deviations are ignored, only qualitative statements can be made about the spatial and metallicity distributions of halo stars – beyond 30 kpc, the spatial distribution is probably steeper than a $1/r^3$ power law, and the median metallicity is likely lower by 0.3-0.5 dex than the value of $[Fe/H] \sim -1.5$ representative for the inner halo (based on BHB stars, see Xue et al. 2008; Beers

et al. 2011). Indirect evidence suggests that the outer halo possesses a retrograde net rotation; this result should be checked by further study.

More robust results exist for the behavior of the halo radial-velocity dispersion out to ~ 100 kpc. Battaglia et al. (2005) used a heterogeneous sample of 240 objects (globular clusters, satellite galaxies, BHB stars, red giants), and measured a decrease in radial-velocity dispersion from 120 km s^{-1} at 30 kpc to about 80 km s^{-1} at 100 kpc (these authors also claim 50 km s^{-1} at 120 kpc, but there are only four objects beyond 100 kpc in their sample). Using about 2400 BHB stars detected by SDSS out to 60 kpc, Xue et al. (2008) measured a slightly lower velocity dispersion than Battaglia et al. (e.g., $\sim 100 \text{ km s}^{-1}$ at 30 kpc vs. 120 km s^{-1}), and a shallower gradient by about a factor of two (e.g., their best fit implies a drop of 18 km s^{-1} , or 18%, between 30 kpc and 100 kpc, compared to a drop of 40 km s^{-1} , or 33%, in Battaglia et al.). Brown et al. (2010) used a mix of 910 BHB and blue straggler stars from the Hypervelocity Star survey to measure the halo radial-velocity dispersion out to 75 kpc. They obtained results in statistical agreement with Battaglia et al. (2005) and Xue et al. (2008), which they summarized as (see their Figure 7 for a pictorial summary) “the Milky Way radial-velocity dispersion drops from $\sigma = 110 \text{ km s}^{-1}$ at $R_{gc} = 15 \text{ kpc}$ to $\sigma = 85 \text{ km s}^{-1}$ at $R_{gc} = 80 \text{ kpc}$.” (R_{gc} is the Galactocentric radius).

In contrast, De Propris, Harrison & Mares (2010) used ~ 700 BHB stars from the 2Qz Redshift Survey, and found a very strong increase in the radial-velocity dispersion from 100 km s^{-1} at 30 kpc to 200 km s^{-1} at 80-100 kpc. Furthermore, their dispersion value of $\sim 150 \text{ km s}^{-1}$ at 60 kpc is significantly different from the 94 km s^{-1} obtained by Xue et al. (2008) using the same tracer population. The value of $\sim 150 \text{ km s}^{-1}$ at 60 kpc seems completely ruled out by other studies (e.g.,

see Figure 7 in Brown et al. 2010).

Currently, there are no in situ measurements of tangential velocity dispersion for stars from the outer halo. As discussed above, the difference between σ_Φ and σ_θ is an important measurement for understanding the gravitational potential and stellar distribution in the halo. It seems that such measurements will be possible for post-main-sequence stars with Gaia. For example, a star with $M_r = 1$ would have SDSS r -band magnitude of 19 at a distance of 40 kpc. The expected proper-motion error from Gaia is ~ 0.1 mas yr $^{-1}$ for such a star (see §8), and corresponds to a velocity error of 20 km s $^{-1}$. Such an error is sufficiently small to enable detailed mapping of σ_Φ and σ_θ , based on enormous numbers of distant BHB and red-giant stars.

The chemistry of the outer-halo population, and its differences with respect to the inner-halo population, has only begun to be explored. Present evidence indicates that the diversity of stellar abundance ratios is far greater for members of the outer halo than for the inner halo (see the Introduction of Carollo et al. 2011). The most striking chemical differences between the inner- and outer-halo populations may be revealed by the recently recognized contrast in the frequency of so-called carbon-enhanced metal-poor (CEMP) stars by Carollo et al. (2011). These authors have argued that the previously recognized increase in the frequency of CEMP stars with declining metallicity is due to the fact that the outer-halo component of the Galaxy possesses about twice the fraction of CEMP stars, relative to carbon-normal stars, at a given low metallicity, than the inner-halo component. In their view, the observed correlation is a manifestation of the lower metallicity of outer-halo stars, which begin to dominate halo samples at low abundance. This idea can also account for the observed increase in the fraction

of CEMP stars, at a given metallicity, as a function of height above the Galactic plane (Carollo et al. 2011, Frebel et al. 2006), a result that would be difficult to understand in the context of a single-halo population.

In summary, the outer parts of the halo, beyond ~ 30 kpc from the Galactic center, probably have a steeper density distribution ($n > 3$) and lower median metallicity ($[Fe/H] < -1.5$) than the inner halo. The outer halo appears to be less “squashed” than the inner halo, likely exhibits a net retrograde rotation, and its radial-velocity dispersion probably decreases with Galactocentric distance. There appear to be clear differences in the chemistry of outer-halo stars relative to those of the inner halo. And, as discussed in the next section, both fine and coarse substructure in the outer halo appears much more prominent than in the inner halo.

6.4 Streams and Other Substructure

Was the Milky Way halo, or at least its outer parts, actually assembled from many merged satellite galaxies? Within the framework of hierarchical galaxy formation (Freeman & Bland-Hawthorn 2002), the spheroidal component of the luminous matter should reveal substructures, such as tidal tails and streams (Bullock, Kravtsov & Weinberg 2001; Harding et al. 2001; Helmi & White 1999; Johnston, Hernquist & Bolte 1996). Substructures are expected to be ubiquitous in the outer halo (Galactocentric radii beyond 15-20 kpc), where the dynamical timescales are sufficiently long for them to remain spatially coherent (Johnston, Hernquist & Bolte 1996; Mayer et al. 2002), and indeed many have been discovered during the last decade, the famous “Field of Streams” (Belokurov et al. 2006a) is shown in Figure 18.

The tidal streams of the disrupting Sagittarius dwarf spheroidal galaxy (Ibata, Gilmore & Yanny et al. 2000), and they are still the best examples of such substructures, with the streams wrapping around most of the sky (Ibata et al. 2001b, Majewski et al. 2003). Other known substructures include the Virgo Stellar Stream (Duffau et al. 2006, Prior et al. 2009), and several other small and large structures associated with the Virgo overdensity (Newberg et al. 2007, Vivas et al. 2008, Juric08), the Monoceros structure (Ibata et al. 2003, Rocha-Pinto et al. 2003, Yanny et al. 2003, Ivezić08), the Triangulum-Andromeda overdensity (Rocha-Pinto et al. 2004b), the Hercules-Aquila cloud (Belokurov et al. 2007a), the Pisces overdensity (Kollmeier et al. 2009, Sesar et al. 2010a, 2007, 2010b, Watkins et al. 2009), the Orphan stream (Belokurov et al. 2007c, 2006b, Clewley & Kinman 2006, Newberg et al. 2002, Starkenburg et al. 2009, Vivas & Zinn 2006) and streams (Grillmair 2009, Grillmair & Dionatos 2006, Klement et al. 2009, Klement 2010, Schlafman et al. 2009). Similar abundant substructure has been detected in the M31 halo (Ferguson et al. 2002, Ibata et al. 2001a). Last but not least, the SDSS imaging data have enabled a large number of new discoveries of dwarf galaxy companions to the Milky Way, with luminosities as small as 10^{-7} of the Milky Way luminosity (for an up-to-date review, see Willman 2010).

These substructures exhibit various degrees of contrast with respect to the background counts, metallicity, and kinematic distributions of the smooth halo. Bell et al. (2010) used a novel method for investigating differences in age and metallicity between different halo substructures: the ratios of counts of BHB

⁹We note that no clear stellar component has been associated with the Magellanic Stream yet, despite searches for it (Cioni et al. 2011, Moore & Davis 1994, Saha et al. 2010, Westerlund 1990).

stars to main-sequence turnoff stars. Using SDSS data across a quarter of the sky, they found large variations of this ratio, with some halo features almost completely devoid of BHB stars. The Monoceros stream is a good example of substructure that simultaneously deviates from the background distributions in all three observables (see Figure 19). Originally interpreted as a ring around the Galaxy (Ibata et al. 2003, Yanny et al. 2003), it was later revealed as an inclined stream that rotates faster than the surrounding stars, and has a metallicity distribution between those of disk and halo stars (Rocha-Pinto et al. 2003, Juric08, Ivezić08).

The discoveries of abundant substructure represent ample evidence that the Milky Way halo is a very complex structure that holds important clues for deciphering the processes that governed its formation and evolution. Yet, despite this menagerie of substructure, we still do not have a consensus answer for as simple a question as “What fraction of halo stars was accreted from merged galaxies?” Of course, questions about the luminosity and metallicity distributions of the merged galaxies are even more open. A part of the problem is that, within the neighborhood of strong individual substructures, such as those listed above, it is hard to define the “smooth” background, and when strong substructure is absent, it is hard to find weaker features. Several approaches to quantifying the amount of halo substructure have been taken in recent years.

Three studies compared the spatial distribution of SDSS stars, with distances based on photometric parallax methods, to estimates of the smooth background, and used variations (the root-mean-square deviation, rms scatter) of the measured density around that background as a quantitative measure of substructure. The Juric08 approach used their best-fit smooth models for the background es-

timate, and ruled out significant clumpiness on spatial scales comparable to the pixel size of their maps (ranging from 25 pc to 500 pc). On the other hand, Bell et al. (2008) compared the spatial distribution of SDSS stars to that from simulations where the halo is composed entirely of disrupted satellites, and found them to be similar for Galactocentric radii less than 40 kpc. They argued that no smooth model can describe the data, and concluded that the stellar halo is dominated by substructure, with the rms scatter, relative to smooth models on spatial scales above 100 pc, of at least 40%. The Bell et al. study relied on SDSS observations of main-sequence stars and pushed the data all the way to its faint limit ($r \sim 22.5$). Deason, Belokurov & Evans (2011) instead used BHB and blue-straggler stars from SDSS DR8 to study their distribution to a similar distance limit of 40 kpc, but with much brighter stars. They reported for their smooth models that the rms scatter of the data around the maximum likelihood model typically ranges between 5% and 20%. They concluded that “This indicates that the Milky Way stellar halo, or at least the component traced by the A-type stars in the SDSS DR8, is smooth and not dominated by unrelaxed substructure.”. It should be kept in mind that this inference reflects the present situation, and may not apply to the situation at earlier times. Using RR Lyrae stars from SDSS Stripe 82, Sesar et al. (2010a) found that “At least 20% of halo stars within 30 kpc from the Galactic center can be statistically associated with substructure.” And further, that “...beyond a Galactocentric distance of ~ 30 kpc, a larger fraction of the stars are associated with substructure.” (see Figure 20).

The addition of kinematic data increases the contrast ratio relative to the smooth background when searching for substructure. Using data from the SEGUE spectroscopic survey, Schlaufman et al. (2009) have shown that metal-poor main-

sequence turnoff stars within ~ 20 kpc from the Sun exhibit clear evidence for radial velocity clustering on very small spatial scales (dubbed “ECHOS” for Elements of Cold Halo Substructure; see the bottom panel in Figure 14). They estimated that about 10% of the inner halo turnoff stars belong to ECHOS, and inferred the existence of about 1000 ECHOS in the entire inner halo. Their “result suggests that the level of merger activity has been roughly constant over the past few Gyr and that there has been no accretion of single stellar systems more massive than a few percent of a Milky Way mass in that interval.”

Schlafman et al. (2011) argue that the most likely progenitors of ECHOS are dwarf spheroidal galaxies. Typical values of metallicity ($[Fe/H] \sim -1$) and radial-velocity dispersion ($\sim 20 \text{ km s}^{-1}$) for ECHOS imply a dwarf galaxy mass of about $10^9 M_{\odot}$. Theoretical predictions that prominent halo substructures are likely to be metal-rich (Bullock & Johnston 2005, Font et al. 2008) are consistent with the typical ECHOS metallicity, as well as with the measurements reported for the Monoceros stream ($[Fe/H] = -1.0$, Ivezić08) and the trailing part of the Sagittarius tidal stream ($[Fe/H] = -1.2$, Sesar et al. 2010a).

Smith et al. (2009) used the full phase-space coordinates for a sample of some 1700 SDSS subdwarfs, and found evidence for four discrete overdensities localized in angular momentum space, which they dubbed Sloan Kinematic Overdensities (SKOs). One of them was identified earlier in the pioneering work by Helmi et al. (1999), and two new substructures contain stars that are localized in both kinematics and metallicity. One of them has metallicity lower than that of halo background by ~ 0.5 dex, and appears to be related with an association of four globular clusters (NGC5466, NGC6934, NGC7089/M2 and NGC6205/M13), suggesting that they may have been part of the same accretion event. If so, then

this implies that the progenitor must have been a large satellite, similar in size to Fornax.

Xue et al. (2011) analyzed kinematic data for a sample of over 4000 BHB stars detected by SDSS at distances 5-40 kpc. Using a method developed for the analysis of data from the Spaghetti project (Starkenburg et al. 2009), they found an excess of stars that are both close neighbors and have similar radial velocities, compared to a distribution expected for a random sample. Notably, the excess is larger for a subsample of stars at distances beyond 20 kpc than for the closer subsample. Analogous analysis of mock catalogs from simulations in which the stellar halo is composed entirely of disrupted satellite debris exhibits a similar, though somewhat less prominent, level of structure. In a separate study, also based on SDSS observations of BHB stars and using a similar analysis method, Cooper et al. (2011) analyzed a large number of state-of-the-art models for the stellar halo. They also found that, for the inner halo, the models predict stronger clustering than observed, suggesting the existence of a smooth component not currently included in their simulations.

In summary, these new studies consistently reveal that the inner region of the Milky Way's stellar halo, within 30 kpc or so, definitely exhibits substructure. Estimates of the fraction of stars that belong to substructures cluster around a few tens of percent. Observations of several luminous tracers of the outer region of the halo, such as RR Lyrae and BHB stars, suggest that the substructure becomes more prominent with increasing distance from the Galactic center, and that the fraction of stars belonging to substructures is higher than for the inner halo. The available data (still) cannot reliably exclude the possibility that practically all stars in the outer halo belong to substructures.

7 UNANSWERED QUESTIONS

It is not difficult to appreciate the progress that has been made, compared to the state of the field and the open questions of only a decade ago. The metallicity distribution of the halo was found to possess a very low-metallicity tail, one that is correlated with kinematics and points to an existence of a separate outer-halo component. The density profile of the halo was shown to be more complex than originally thought, becoming steeper beyond $\sim 25\text{kpc}$, and exhibiting significant substructure. Tens of dwarf galaxies and a number of new streams, some with clear dwarf galaxy progenitors, have been found, proving that the Sgr stream, while still remaining the largest, was in no way a qualitatively unique event. And finally, it has become clear that the thin and thick disks of the Milky Way are demonstrably distinct physical components, separable by their kinematics and $[\alpha/Fe]$ ratios, and mapped and measured in exquisite detail. Thus we argue that the past decade of large surveys has successfully retired issues #1 through #4, as well as issue #6, mentioned in Section 3.

However, as usually happens, these breakthroughs have left us with new puzzles and questions to ponder over the decade to come. Here, we call attention to only a few:

1. What is the nature, and the formation mechanism, of the two chemically and kinematically separate disk populations? On the most basic level, is the thick disk a result of one or more merger events, or is it a natural consequence of secular evolution and radial migration? If it is the latter, what explains the counter-rotating disks seen in some external galaxies?
2. If the thick disk was formed by mergers, how massive and numerous were

they? What fraction of the thick disk material (if any) has been accreted, and what fraction came from heating of the material already settled into the thin disk (both gas and stars)? Is there even a single thick disk to speak of, or are there multiple intertwined populations tracing their origin to individual merger events? Could this be the explanation of the metal-weak thick disk and the non-Gaussianity of $[Fe/H]$ and $[\alpha/Fe]$ distributions?

3. How do the properties of the bulge compare to those of the disk and the halo?
4. Will the inner/outer halo dichotomy be confirmed by in-situ measurements? Currently, our inferences about the outer-halo population are largely drawn from local kinematically-selected samples. In-situ measurements of the properties of halo stars at $r > 25$ kpc, using large and representative samples, may settle these controversies.
5. Assuming the outer halo is distinct from the inner halo, what are their origins and mechanisms of formation? What (if any) fraction of the outer halo has formed stars in-situ, as opposed to having accreted them? What fraction of the inner halo traces its origin to merger events? What does this tell us about the merger history of the Galaxy?
6. And finally, what is the gravitational potential of the Milky Way's dark matter halo? Multiple lines of evidence currently point to its near-sphericity, a result at odds with expectations for a typical dark matter halo (either prolate or oblate, with $q \sim 0.6$) from N-body simulations.

8 THE ROAD AHEAD

The last decade has seen fascinating observational progress in Milky Way studies. Nevertheless, the results discussed here will be greatly extended by several upcoming large-scale, ground-based projects, including APOGEE, LAMOST, the SkyMapper, Dark Energy Survey, Pan-STARRS, and ultimately the Large Synoptic Survey Telescope. These new surveys¹⁰ will extend the faint limit of the current surveys, such as SDSS, by up to 5 magnitudes. In addition, the upcoming Gaia space mission will provide superb astrometric and photometric measurement accuracy for sources with $r < 20$, and will enable unprecedented science programs. We briefly describe these new surveys, and some of the impact they are expected to have on Milky Way studies.

8.1 SDSS APOGEE Survey

The SDSS-III Apache Point Observatory Galaxy Evolution Experiment (APOGEE) will soon yield unprecedented insight into the chemical and kinematic properties of the main Galactic components, with a unique dataset for studying the bulge (Allende Prieto et al. 2008, Eisenstein et al. 2011, Rockosi et al. 2009, Schiavon & Majewski 2010). The APOGEE project is a three-year high-resolution near-infrared spectroscopic survey that will target over 200 field centers covering about 1200 deg² of sky. The project utilizes a new 300-fiber-fed H -band (1.51 to 1.68 μm) spectrograph with a resolution of $R \sim 20,000$, and expected signal-to-

¹⁰Regretfully, due to space constraints we do not address infrared surveys, such as WISE (Wright et al. 2010), GLIMPSE (Churchwell et al. 2009), VISTA (McPherson et al. 2006), and UKIDSS (Lawrence et al. 2007). These surveys will have a major impact on studies of the Galactic bulge and the dust-obscured regions of the Galactic plane.

noise ratio of 100 per resolution element, for stars with $H \sim 12$ (with the ARC 2.5m telescope used by SDSS). The goal of the survey is to derive precision radial velocities ($\sigma < 1 \text{ km s}^{-1}$) and abundances ($\sigma < 0.1 \text{ dex}$) for about 100,000 stars, targeted using the 2MASS imaging survey (red giants will be observable all the way to the Galactic center). Abundances of 15 different elements, including *Fe*, *C*, *N*, *O*, α -elements, odd-*Z* elements, and iron-peak elements, will be measured.

APOGEE will be the first spectroscopic survey to pierce through the dust obscuration in the Galactic plane (extinction in the near-infrared *H* band is about six times smaller than in the optical *V* band), and provide a large, uniform database of chemical abundances and radial velocities for stars across all of the known Galactic components. These data will provide a robust set of constraints against which chemodynamical models for the formation and evolution of the Galaxy can be tested. In particular, APOGEE will provide powerful new constraints on the nature and influence of the Galactic bar and spiral arms, and will conduct a legacy survey of Galactic open clusters to constrain the history of star formation and chemical enrichment of the Galactic disk (Frinchaboy et al. 2010).

8.2 The LAMOST Galactic Surveys

The Large Area Multi-Object fiber Spectroscopic Telescope (LAMOST) is a 4m-class telescope with 4000 optical fibers in the focal plane, sited at the Xinglong Observatory in northeast China. This telescope, built by the National Astronomical Observatory of China, will carry out a spectroscopic survey of millions of Galactic stars over a five or six year period, expected to start in 2012. The magnitude limit, wavelength range, and spectral resolution of the LAMOST Galactic structure surveys will be similar to that achieved by SEGUE/SDSS.

The stellar science goals, grouped under the LAMOST Experiment for Galactic Understanding and Exploration (LEGUE) effort, are divided into three major parts: (1) The spheroid survey, (2) The Galactic anticenter survey, and (3) The Galactic disk and open clusters survey. The stellar surveys will receive about half of the available time, resulting in a sample of about 6 million bright disk stars, and at least 2 million fainter halo stars. These surveys will result in the largest homogeneous spectroscopic datasets for stars in the Milky Way, with several times more spectra than obtained by the SDSS and RAVE surveys combined.

8.3 SkyMapper, Pan-STARRS, and the Dark Energy Survey

There are three imminent optical surveys that will cover large swaths of the optical sky to faint limits, and are destined to yield many significant discoveries. They are, in many ways, similar to the SDSS imaging survey (including the photometric systems), but they will extend it significantly in sky coverage, imaging depth, and temporal coverage.

8.3.1 SKYMAPPER The SkyMapper (Murphy et al. 2009) is a 1.35m telescope with a 5.7 deg^2 field of view and a 0.27 Gigapixel camera. Its primary goal will be to undertake the Southern Sky Survey: a six band, six-epoch (in each band) digital record of the entire southern sky. The survey will provide astrometry and photometry for objects with $8 < r < 23$. Each of the six epochs will use 110 s exposures that will be about 1 mag shallower than SDSS data, but when co-added, will reach the SDSS depth. The four red bandpasses (*griz*) are designed to be similar to the SDSS bandpasses. SkyMapper has two additional, distinctive ultraviolet filters, a Strömgren system-like *u*-band filter, and a unique narrow *v*-band filter near 4000 \AA . These two filters bracket the Balmer

jump in stellar spectra, and are designed to efficiently identify metal-poor stars (Bessell et al. 2011). The advertised performance requirements include a photometric precision of 0.03 mag globally, and astrometric precision (better than 50 mas) that will enable measured proper motions accurate to about 4 mas yr^{-1} over the five year baseline of the survey.

The SkyMapper’s Southern Sky Survey will extend many of the results based on SDSS imaging survey to the Southern hemisphere, over 20,000 deg^2 of sky (Keller et al. 2007). The photometric parallax methods developed for SDSS data should be directly applicable to SkyMapper’s data, and photometric metallicity methods should perform even better, thanks to the optimized ultraviolet band-passes. The expected proper-motion accuracy is essentially the same as delivered by the SDSS-POSS proper-motion catalog, and thus it will be possible to extend many of the SDSS-based studies described here to essentially the entire sky.

8.3.2 PAN-STARRS The Panoramic Survey Telescope And Rapid Response System (Pan-STARRS; Kaiser et al. 2010) is a wide-field, multi-filter, multi-epoch astronomical survey program. The program is currently based on a 1.8m telescope with a 7 deg^2 field of view and a 1.4 Gigapixel camera (PS1), which began full science operations in 2010. The largest of the PS1 surveys is the 3π Survey, which is planned to cover the 30,000 deg^2 of sky visible from Hawaii ($\delta > -30^\circ$) in five filters (SDSS-like *griz* and *y* at $\sim 1\mu\text{m}$), with pairs of observations in each filter being taken at six different epochs.

PS1 will increase the SDSS sky coverage by a factor of two, and will reach at least a magnitude deeper (with a second telescope, or perhaps all four that are envisioned in this program, the depth gain could be up to another magnitude). Both of these advantages will most likely yield new discoveries in the context

of Milky Way studies. A additional magnitude of depth corresponds to 60% larger distance limit, and could bridge the 25 kpc to 40 kpc range, where the transition between the inner and outer halo is probably taking place, with turn-off stars. In addition, the coverage of the Galactic plane will be much better than with SDSS, and the y -band will be more apt at penetrating through the high ISM dust extinction at low Galactic latitudes. Unfortunately, the Pan-STARRS system does not include an ultraviolet band required for photometric metallicity estimates.

8.3.3 THE DARK ENERGY SURVEY The Dark Energy Survey (DES) will utilize a new 0.52 Gigapixel camera at the 4m Blanco telescope (3.8 deg² field of view) to cover 5000 square degrees of the southern sky (Flaugher 2008). The survey will be completed during a 5-year period starting in 2012, and will include SDSS-like $griz$ passbands and the y -band. Similarly to Pan-STARRS, DES will not include an ultraviolet band. As its name implies, although Milky Way studies are not its primary goal, it will nevertheless provide valuable data.

Although the Dark Energy Survey will cover “only” about 5,000 deg² of the Southern sky, it will reach about 1.5-2 magnitudes deeper than the SkyMapper survey (and SDSS). This depth gain, and corresponding improvement in the limiting distance by a factor of 2-2.5, is likely to bring significant new discoveries, especially in the context of the Galactic halo.

8.4 Gaia

Gaia is an ESA Cornerstone mission set for launch in 2013. Building on experience from HIPPARCOS, it will survey the sky to a magnitude limit of $r \sim 20$ (approximately, see below), and obtain astrometric and three-band photometric

measurements for about 1 billion sources, as well as radial-velocity and chemical-composition measurements (using the 847-874 nm wavelength range) for 150 million stars with $r < 18$ (Perryman 2002, Wilkinson et al. 2005). The final data product, the Gaia Catalogue, is expected to be published by 2020, although early data releases are planned.

Gaia's payload will include two telescopes sharing a common focal plane, with two $1.7^\circ \times 0.6^\circ$ viewing fields separated by a highly stable angle of 106.5° . The focal plane includes a mosaic of 106 CCDs, with a total pixel count close to one billion. Due to the spacecrafts' rotation and precession, the entire sky will be scanned in TDI mode (time-delay-and-integrate, or drift scanning) about 70 times, on average, during 5 years of operations. Gaia will produce broad-band G magnitudes with sensitivity in the wavelength range 330-1020 nm (FWHM points at ~ 400 nm and ~ 850 nm). The spectral energy distribution of each source will be sampled by a spectrophotometric instrument providing low-resolution spectra in the blue (BP , effective wavelength ~ 520 nm) and in the red (RP , effective wavelength ~ 800 nm). In addition, the RVS instrument (radial velocity spectrograph) will disperse the light in the range 847–874 nm, for which it will include a dedicated filter.

8.5 LSST

The Large Synoptic Survey Telescope (LSST) is the most ambitious currently planned wide-field ground-based optical system (Ivezić et al. 2008a). The current baseline design, with an 8.4m primary mirror, a 9.6 deg^2 field of view, and a 3.2 Gigapixel camera, will allow about 20,000 square degrees of sky visible from Cerro Pachón in Northern Chile to be covered to a depth of $r \sim 27.5$ over the 10-year

survey. About 1000 observations (summed over the six bands, *ugrizy*) will be obtained during that period, enabling unprecedented time-domain studies. LSST will obtain proper-motion measurements of comparable accuracy to those of Gaia at its faint limit (and $r \sim 20$), and smoothly extend the error vs. magnitude curve deeper by about 5 mag (see Figure 21).

LSST will produce a massive and exquisitely accurate photometric and astrometric dataset for about 10 billion Milky Way stars. The coverage of the Galactic plane will yield data for numerous star-forming regions, and the *y*-band data will penetrate through the interstellar dust layer. With its *u*-band data, LSST will enable studies of metallicity and kinematics using the same sample of stars out to a distance of ~ 40 kpc (~ 200 million F/G main-sequence stars brighter than $r = 23$; for a discussion see Ivezić08), and the spatial distribution of halo turn-off stars will be traced out to ~ 100 kpc. No other existing or planned survey will provide such a massive and powerful dataset to study the outer halo. The LSST, in its standard surveying mode, will be able to efficiently detect RR Lyrae stars, and hence explore the extent and structure of the halo out to 400 kpc (see Figure 22). All together, the LSST will enable studies of the stellar distribution beyond the presumed edge of the Galactic halo, of their metallicity distribution throughout most of the halo, and of their kinematics beyond the thick disk/halo boundary (for more detailed discussion see the LSST Science Book; LSST Science Collaborations et al. 2009).

8.6 The Synergy between Gaia and LSST

In the context of Gaia, the LSST can be thought of as its deep complement. A detailed comparison of LSST and Gaia performance is given in Figure 21. Gaia

will provide an all-sky catalog with unsurpassed trigonometric parallax, proper-motion, and photometric measurements to $r \sim 20$, for about 10^9 stars. LSST will extend this map to $r \sim 27$ over half of the sky, detecting about 10^{10} stars. Because of Gaia’s superb astrometric and photometric quality, and LSST’s significantly deeper reach, the two surveys are highly complementary – Gaia will map the Milky Way’s disk with unprecedented detail, and LSST will extend this map all the way to the edge of the known halo and beyond.

A quantitative comparison of the distance-color coverage for main-sequence stars by Gaia and LSST is shown in Figure 23. For example, stars just below the main-sequence turn-off, with $M_r = 4.5$, will be detected by Gaia to a distance limit of ~ 10 kpc ($r < 20$), and to ~ 100 kpc with LSST’s single-epoch data ($r < 24.5$). For intrinsically faint stars, such as late M dwarfs, L/T dwarfs, and white dwarfs, the deeper limit of LSST will enable detection and characterization of the halo populations. A star with $M_r = 15$ will be detectable to a distance limit of 100 pc with Gaia and ~ 800 pc with LSST, hence the LSST samples will be about 100 times larger. In addition, for a substantial fraction of red stars with $r > 20$, LSST will provide trigonometric parallax measurements accurate to better than 10%. Hence, despite the unprecedented performance of Gaia for $r < 20$, LSST will enable major discoveries with its deep $r > 20$ sky coverage. At the same time, and in addition to its own discoveries, Gaia will provide excellent astrometric and photometric calibration samples for LSST. To conclude, “these are exciting times to study local galaxies” (Wyse 2006).

Table 1: The Best-fit Parameters for the Juric08 Galactic Model^a

Parameter	Measured	Bias-corrected	Error estimate
Z_0	25	...	20%
L_1	2150	2600	20%
H_1	245	300	20%
f_d	0.13	0.12	10%
L_2	3261	3600	20%
H_2	743	900	20%
f_h	0.0051	...	25%
q	0.64	...	≤ 0.1
n	2.77	...	≤ 0.2

^a Best-fit Galactic model parameters from Juric08, as directly measured from the apparent number-density distribution maps (2nd column), after correcting for a 35% assumed binary fraction and Malmquist bias due to photometric errors and dispersion around the mean of the photometric parallax relation (3rd column). Z_\odot is the Solar offset from the Galactic plane (pc), H_1 , H_2 and L_1 , L_2 (pc) are the scale heights and lengths for the thin and thick disk, respectively, f_d and f_h are the thick disk and halo normalizations relative to the thin disk at ($R = R_\odot, Z = 0$), q parametrizes the halo ellipticity (with the ellipsoid described by axes $a = b$ and $c = qa$; for $q < 1$ the halo is oblate, that is, “squashed” in the same sense as the disk), and n is the power-law index for the halo number-density profile.

References

1. Aihara H, Allende Prieto C, An D, Anderson SF, Aubourg É, et al. 2011. *Astrophysical Journal Supplement* 193:29–+
2. Allende Prieto C, Beers TC, Wilhelm R, Newberg HJ, Rockosi CM, et al. 2006. *Astrophysical Journal* 636:804–820
3. Allende Prieto C, Majewski SR, Schiavon R, Cunha K, Frinchaboy P, et al. 2008. *Astronomische Nachrichten* 329:1018–+
4. Bahcall JN, Soneira RM. 1980. *Astrophysical Journal Supplement* 44:73–110
5. Battaglia G, et al. 2005. *Monthly Notices of the R.A.S.* 364:433–442
6. Beers TC, Carollo D, Ivezić Z, An D, Chiba M, et al. 2011. ArXiv:1104.2513
(accepted to *ApJ*)
7. Beers TC, Chiba M, Yoshii Y, Platais I, Hanson RB, et al. 2000. *Astronomical Journal* 119:2866–2881
8. Beers TC, Christlieb N. 2005. *Annu. Rev. Astro. Astrophys.* 43:531–580
9. Beers TC, Lee Y, Sivarani T, Allende Prieto C, Wilhelm R, et al. 2006. *Mem.S.A.It.* 77:1171–+
10. Beers TC, Preston GW, Shectman SA. 1992. *Astronomical Journal* 103:1987–2034
11. Bell EF, Xue XX, Rix HW, Ruhland C, Hogg DW. 2010. *Astronomical Journal* 140:1850–1859
12. Bell EF, Zucker DB, Belokurov V, Sharma S, Johnston KV, et al. 2008. *Astrophysical Journal* 680:295–311

13. Belokurov V, Evans NW, Bell EF, Irwin MJ, Hewett PC, et al. 2007a.
Astrophysical Journal Letters 657:L89–L92
14. Belokurov V, Evans NW, Irwin MJ, Lynden-Bell D, Yanny B, et al. 2007b.
Astrophysical Journal 658:337–344
15. Belokurov V, Zucker DB, Evans NW, Gilmore G, Vidrih S, et al. 2006a.
Astrophysical Journal Letters 642:L137–L140
16. Belokurov V, Zucker DB, Evans NW, Kleyana JT, Koposov S, et al. 2007c.
Astrophysical Journal 654:897–906
17. Belokurov V, Zucker DB, Evans NW, Wilkinson MI, Irwin MJ, et al. 2006b.
Astrophysical Journal Letters 647:L111–L114
18. Bensby T, Feltzing S, Lundström I. 2004. *Astronomy & Astrophysics* 421:969–976
19. Bessell M, Bloxham G, Schmidt B, Keller S, Tisserand P, Francis P. 2011. *PASP*
123:789–798
20. Boeche C, Siebert A, Williams M, de Jong RS, Steinmetz M, et al. 2011.
ArXiv:1109.5670
21. Bond NA, Ivezić Ž, Sesar B, Jurić M, Munn JA, et al. 2010. *Astrophysical Journal*
716:1–29
22. Bonifacio P, Centurion M, Molaro P. 1999. *Monthly Notices of the R.A.S.*
309:533–542
23. Bovy J, Rix HW, Hogg DW. 2011. *ArXiv:1111.6585*
24. Brook C, Richard S, Kawata D, Martel H, Gibson BK. 2007.
Astrophysical Journal 658:60–64
25. Brook CB, Gibson BK, Martel H, Kawata D. 2005. *Astrophysical Journal*
630:298–308

26. Brown WR, Geller MJ, Kenyon SJ, Diaferio A. 2010. *Astronomical Journal* 139:59–67
27. Bullock JS, Dekel A, Kolatt TS, Kravtsov AV, Klypin AA, et al. 2001. *Astrophysical Journal* 555:240–257
28. Bullock JS, Johnston KV. 2005. *Astrophysical Journal* 635:931–949
29. Bullock JS, Kravtsov AV, Weinberg DH. 2001. *Astrophysical Journal* 548:33–46
30. Burnett B, Binney J, Sharma S, Williams M, Zwitter T, et al. 2011. *Astronomy & Astrophysics* 532:A113+
31. Cabrera-Lavers A, González-Fernández C, Garzón F, Hammersley PL, López-Corredoira M. 2008. *Astronomy & Astrophysics* 491:781–787
32. Carney BW, Laird JB, Latham DW, Aguilar LA. 1996. *Astronomical Journal* 112:668–+
33. Carollo D, Beers TC, Bovy J, Sivarani T, Norris JE, et al. 2011. ArXiv:1103.3067
34. Carollo D, Beers TC, Chiba M, Norris JE, Freeman KC, et al. 2010. *Astrophysical Journal* 712:692–727
35. Carollo D, et al. 2007. *Nature* 450:1020–1025
36. Casetti-Dinescu DI, Girard TM, Korchagin VI, van Altena WF. 2011. *Astrophysical Journal* 728:7–+
37. Chiba M, Beers TC. 2000. *Astronomical Journal* 119:2843–2865
38. Churchwell E, Babler BL, Meade MR, Whitney BA, Benjamin R, et al. 2009. *PASP* 121:213–230
39. Cioni MRL, Clementini G, Girardi L, Guandalini R, Gullieuszik M, et al. 2011. *Astronomy & Astrophysics* 527:A116

40. Clarkson W, Sahu K, Anderson J, Smith TE, Brown TM, et al. 2008. *Astrophysical Journal* 684:1110–1142
41. Clewley L, Kinman TD. 2006. *Monthly Notices of the R.A.S.* 371:L11–L15
42. Cooper AP, Cole S, Frenk CS, Helmi A. 2011. *Monthly Notices of the R.A.S.* :1440–+
43. Covey KR, Ivezić Ž, Schlegel D, Finkbeiner D, Padmanabhan N, et al. 2007. *Astronomical Journal* 134:2398–2417
44. De Lucia G, Helmi A. 2008. *Monthly Notices of the R.A.S.* 391:14–31
45. De Propriis R, Harrison CD, Mares PJ. 2010. *Astrophysical Journal* 719:1582–1587
46. Deason AJ, Belokurov V, Evans NW. 2011. *Monthly Notices of the R.A.S.* 416:2903–2915
47. Di Matteo P, Lehnert MD, Qu Y, van Driel W. 2011. *Astronomy & Astrophysics* 525:L3+
48. Dierickx M, Klement R, Rix HW, Liu C. 2010. *Astrophysical Journal Letters* 725:L186–L190
49. Dong R, Gunn J, Knapp G, Rockosi C, Blanton M. 2011. *Astronomical Journal* 142:116–+
50. Duffau S, Zinn R, Vivas AK, Carraro G, Méndez RA, et al. 2006. *Astrophysical Journal Letters* 636:L97–L100
51. Eggen OJ, Lynden-Bell D, Sandage AR. 1962. *Astrophysical Journal* 136:748–+
52. Eisenstein DJ, Weinberg DH, Agol E, Aihara H, Allende Prieto C, et al. 2011. *Astronomical Journal* 142:72–+

53. Fellhauer M, Belokurov V, Evans NW, Wilkinson MI, Zucker DB, et al. 2006. *Astrophysical Journal* 651:167–173
54. Ferguson AMN, Irwin MJ, Ibata RA, Lewis GF, Tanvir NR. 2002. *Astronomical Journal* 124:1452–1463
55. Flaugher B. 2008. In *A Decade of Dark Energy: Spring Symposium, Proceedings of the conferences held May 5-8, 2008 in Baltimore, Maryland. (USA). Edited by Norbert Pirzkal and Henry Ferguson.* <http://www.stsci.edu/institute/conference/spring2008>
56. Font AS, Johnston KV, Ferguson AMN, Bullock JS, Robertson BE, et al. 2008. *Astrophysical Journal* 673:215–225
57. Font AS, McCarthy IG, Crain RA, Theuns T, Schaye J, et al. 2011. *Monthly Notices of the R.A.S.* 416:2802–2820
58. Frebel A, Christlieb N, Norris JE, Beers TC, Bessell MS, et al. 2006. *Astrophysical Journal* 652:1585–1603
59. Freeman K, Bland-Hawthorn J. 2002. *Annu. Rev. Astro. Astrophys.* 40:487–537
60. Freeman KC. 1987. *Annu. Rev. Astro. Astrophys.* 25:603–632
61. Frinchaboy P, Zasowski G, Jackson K, Johnson JA, Majewski SR, et al. 2010. In *JENAM 2010, Joint European and National Astronomy Meeting*
62. Fullbright JP, Wyse RFG, Ruchti GR, Gilmore GF, Grebel E, et al. 2010. *Astrophysical Journal Letters* 724:L104–L108
63. Ghigna S, Moore B, Governato F, Lake G, Quinn T, Stadel J. 2000. *Astrophysical Journal* 544:616–628
64. Gilmore G, Reid N. 1983. *Monthly Notices of the R.A.S.* 202:1025–1047

65. Gilmore G, Wyse RFG, Kuijken K. 1989. *Annu. Rev. Astro. Astrophys.* 27:555–627
66. Gonzalez OA, Rejkuba M, Zoccali M, Hill V, Battaglia G, et al. 2011. *Astronomy & Astrophysics* 530:A54+
67. Governato F, Mayer L, Wadsley J, Gardner JP, Willman B, et al. 2004. *Astrophysical Journal* 607:688–696
68. Governato F, Willman B, Mayer L, Brooks A, Stinson G, et al. 2007. *Monthly Notices of the R.A.S.* 374:1479–1494
69. Grillmair CJ. 2009. *Astrophysical Journal* 693:1118–1127
70. Grillmair CJ, Dionatos O. 2006. *Astrophysical Journal Letters* 643:L17–L20
71. Harding P, Morrison HL, Olszewski EW, Arabadjis J, Mateo M, et al. 2001. *Astronomical Journal* 122:1397–1419
72. Hartwick FDA. 1987. In *NATO ASIC Proc. 207: The Galaxy*, ed. G. Gilmore & B. Carswell
73. Helmi A. 2004. *Astrophysical Journal Letters* 610:L97–L100
74. Helmi A. 2008. *AAPR?* 15:145–188
75. Helmi A, White SDM. 1999. *Monthly Notices of the R.A.S.* 307:495–517
76. Helmi A, White SDM, de Zeeuw PT, Zhao H. 1999. *Nature* 402:53–55
77. Ibata R, Irwin M, Lewis G, Ferguson AMN, Tanvir N. 2001a. *Nature* 412:49–52
78. Ibata R, Lewis GF, Irwin M, Totten E, Quinn T. 2001b. *Astrophysical Journal* 551:294–311
79. Ibata RA, Gilmore G, Irwin MJ. 1994. *Nature* 370:194–196

80. Ibata RA, Irwin MJ, Lewis GF, Ferguson AMN, Tanvir N. 2003. *Monthly Notices of the R.A.S.* 340:L21–L27
81. Ivezić Ž, Goldston J, Finlator K, Knapp GR, Yanny B, et al. 2000. *Astronomical Journal* 120:963–977
82. Ivezić Ž, Lupton R, Schlegel D, Smolčić V, Johnston D, et al. 2004. In *Satellites and Tidal Streams*, ed. F. Prada, D. Martinez Delgado, & T. J. Mahoney, vol. 327 of *Astronomical Society of the Pacific Conference Series*
83. Ivezić Ž, et al. 2008a. ArXiv:0805.2366
84. Ivezić Ž, et al. 2008b. *Astrophysical Journal* 684:287–325 (Ivezic08)
85. Johnston KV, Bullock JS, Sharma S, Font A, Robertson BE, Leitner SN. 2008. *Astrophysical Journal* 689:936–957
86. Johnston KV, Hernquist L, Bolte M. 1996. *Astrophysical Journal* 465:278–+
87. Jurić M, et al. 2008. *Astrophysical Journal* 673:864–914
88. Kaiser N, Burgett W, Chambers K, Denneau L, Heasley J, et al. 2010. In *Society of Photo-Optical Instrumentation Engineers (SPIE) Conference Series*, vol. 7733 of *Society of Photo-Optical Instrumentation Engineers (SPIE) Conference Series*
89. Keller SC, Murphy S, Prior S, Da Costa G, Schmidt B. 2008. *Astrophysical Journal* 678:851–864
90. Keller SC, Schmidt BP, Bessell MS, Conroy PG, Francis P, et al. 2007. *PASA* 24:1–12
91. Klement R, et al. 2009. *Astrophysical Journal* 698:865–894
92. Klement RJ. 2010. *AAPR?* 18:567–594

93. Kollmeier JA, Gould A, Shectman S, Thompson IB, Preston GW, et al. 2009.
Astrophysical Journal Letters 705:L158–L162
94. Law DR, Johnston KV, Majewski SR. 2005. *Astrophysical Journal* 619:807–823
95. Lawrence A, Warren SJ, Almaini O, Edge AC, Hambly NC, et al. 2007.
Monthly Notices of the R.A.S. 379:1599–1617
96. Lee YS, Beers TC, Allende Prieto C, Lai DK, Rockosi CM, et al. 2011a.
Astronomical Journal 141:90–+
97. Lee YS, Beers TC, An D, Ivezić Z, Just A, et al. 2011b. ArXiv:1104.3114
98. Lee YS, Beers TC, Sivarani T, Allende Prieto C, Koesterke L, et al. 2008a.
Astronomical Journal 136:2022–2049
99. Lee YS, Beers TC, Sivarani T, Johnson JA, An D, et al. 2008b.
Astronomical Journal 136:2050–2069
100. Loebman SR, Roškar R, Debattista VP, Ivezić Ž, Quinn TR, Wadsley J. 2011.
Astrophysical Journal 737:8–+
101. LSST Science Collaborations, Abell PA, Allison J, Anderson SF, Andrew JR,
et al. 2009. ArXiv:0912.0201
102. Majewski SR. 1992. *Astrophysical Journal Supplement* 78:87–152
103. Majewski SR. 1993. *Annu. Rev. Astro. Astrophys.* 31:575–638
104. Majewski SR. 2010. In *IAU Symposium*, ed. G. Bruzual & S. Charlot, vol. 262
of *IAU Symposium*
105. Majewski SR, Skrutskie MF, Weinberg MD, Ostheimer JC. 2003.
Astrophysical Journal 599:1082–1115
106. Mayer L, Moore B, Quinn T, Governato F, Stadel J. 2002.
Monthly Notices of the R.A.S. 336:119–130

107. McPherson AM, Born A, Sutherland W, Emerson J, Little B, et al. 2006. In *Society of Photo-Optical Instrumentation Engineers (SPIE) Conference Series*, vol. 6267 of *Society of Photo-Optical Instrumentation Engineers (SPIE) Conference Series*
108. Miceli A, Rest A, Stubbs CW, Hawley SL, Cook KH, et al. 2008. *Astrophysical Journal* 678:865–887
109. Minchev I, Famaey B. 2010. *Astrophysical Journal* 722:112–121
110. Minniti D, Zoccali M. 2008. In *IAU Symposium*, ed. M. Bureau, E. Athanassoula, & B. Barbuy, vol. 245 of *IAU Symposium*
111. Monet DG, Levine SE, Canzian B, Ables HD, Bird AR, et al. 2003. *Astronomical Journal* 125:984–993
112. Moore B, Davis M. 1994. *Monthly Notices of the R.A.S.* 270:209
113. Morrison HL, Flynn C, Freeman KC. 1990. *Astronomical Journal* 100:1191–1222
114. Munn JA, et al. 2004. *Astronomical Journal* 127:3034–3042
115. Murphy S, Keller S, Schmidt B, Tisserand P, Bessell M, et al. 2009. In *The Eighth Pacific Rim Conference on Stellar Astrophysics: A Tribute to Kam-Ching Leung*, ed. S. J. Murphy & M. S. Bessell, vol. 404 of *Astronomical Society of the Pacific Conference Series*
116. Newberg HJ, Yanny B, Cole N, Beers TC, Re Fiorentin P, et al. 2007. *Astrophysical Journal* 668:221–235
117. Newberg HJ, Yanny B, Grebel EK, Hennessy G, Ivezić Ž, et al. 2003. *Astrophysical Journal Letters* 596:L191–L194
118. Newberg HJ, Yanny B, Rockosi C, Grebel EK, Rix HW, et al. 2002. *Astrophysical Journal* 569:245–274

119. Nordström B, Mayor M, Andersen J, Holmberg J, Pont F, et al. 2004. *Astronomy & Astrophysics* 418:989–1019
120. Norris J. 1986. *Astrophysical Journal Supplement* 61:667–698
121. Norris J, Bessell MS, Pickles AJ. 1985. *Astrophysical Journal Supplement* 58:463–492
122. Norris JE, Ryan SG. 1991. *Astrophysical Journal* 380:403–418
123. Perryman MAC. 2002. *Astronomy & Astrophysics Supp. Ser.* 280:1–10
124. Perryman MAC, Lindegren L, Kovalevsky J, Hoeg E, Bastian U, et al. 1997. *Astronomy & Astrophysics* 323:L49–L52
125. Pont F, Eyer L. 2004. *Monthly Notices of the R.A.S.* 351:487–504
126. Pourbaix D, Knapp GR, Szkody P, Ivezić Ž, Kleinman SJ, et al. 2005. *Astronomy & Astrophysics* 444:643–649
127. Preston GW, Shectman SA, Beers TC. 1991. *Astrophysical Journal* 375:121–147
128. Prior SL, Da Costa GS, Keller SC, Murphy SJ. 2009. *Astrophysical Journal* 691:306–319
129. Rangwala N, Williams TB. 2009. *Astrophysical Journal* 702:414–424
130. Rangwala N, Williams TB, Stanek KZ. 2009. *Astrophysical Journal* 691:1387–1399
131. Rattenbury NJ, Mao S, Sumi T, Smith MC. 2007. *Monthly Notices of the R.A.S.* 378:1064–1078
132. Rich RM. 2011. In *RR Lyrae Stars, Metal-Poor Stars, and the Galaxy*, ed. A. McWilliam
133. Robin AC, Marshall DJ, Schultheis M, Reyle C. 2011. ArXiv:1111.5744

134. Robin AC, Reylé C, Derrière S, Picaud S. 2003. *Astronomy & Astrophysics* 409:523–540
135. Rocha-Pinto HJ, Flynn C, Scalo J, Hänninen J, Maciel WJ, Hensler G. 2004a. *Astronomy & Astrophysics* 423:517–535
136. Rocha-Pinto HJ, Majewski SR, Skrutskie MF, Crane JD. 2003. *Astrophysical Journal Letters* 594:L115–L118
137. Rocha-Pinto HJ, Majewski SR, Skrutskie MF, Crane JD, Patterson RJ. 2004b. *Astrophysical Journal* 615:732–737
138. Rockosi C, Beers TC, Majewski S, Schiavon R, Eisenstein D. 2009. In *astro2010: The Astronomy and Astrophysics Decadal Survey*, vol. 2010 of *Astronomy*
139. Roškar R, Debattista VP, Quinn TR, Stinson GS, Wadsley J. 2008a. *Astrophysical Journal Letters* 684:L79–L82
140. Roškar R, Debattista VP, Stinson GS, Quinn TR, Kaufmann T, Wadsley J. 2008b. *Astrophysical Journal Letters* 675:L65–L68
141. Ruchti GR, Fulbright JP, Wyse RFG, Gilmore GF, Bienaymé O, et al. 2011. *Astrophysical Journal* 737:9–+
142. Ryan SG, Lambert DL. 1995. *Astronomical Journal* 109:2068–+
143. Ryan SG, Norris JE. 1991. *Astronomical Journal* 101:1865–1878
144. Saha A, Olszewski EW, Brondel B, Olsen K, Knezek P, et al. 2010. *Astronomical Journal* 140:1719–1738
145. Sales LV, Helmi A, Abadi MG, Brook CB, Gómez FA, et al. 2009. *Monthly Notices of the R.A.S.* 400:L61–L65
146. Schiavon RP, Majewski SR. 2010. In *IAU Symposium*, ed. G. Bruzual & S. Charlot, vol. 262 of *IAU Symposium*

147. Schlafman KC, Rockosi CM, Allende Prieto C, Beers TC, Bizyaev D, et al. 2009.
Astrophysical Journal 703:2177–2204
148. Schlafman KC, Rockosi CM, Lee YS, Beers TC, Allende Prieto C. 2011.
Astrophysical Journal 734:49–+
149. Schönrich R. 2011. ArXiv:1111.3651
150. Schönrich R, Asplund M, Casagrande L. 2011. *Monthly Notices of the R.A.S.*
415:3807–3823
151. Schönrich R, Binney J. 2009a. *Monthly Notices of the R.A.S.* 396:203–222
152. Schönrich R, Binney J. 2009b. *Monthly Notices of the R.A.S.* 399:1145–1156
153. Schwarzschild M, Searle L, Howard R. 1955. *Astrophysical Journal* 122:353–+
154. Searle L, Zinn R. 1978. *Astrophysical Journal* 225:357–379
155. Sellwood JA, Binney JJ. 2002. *Monthly Notices of the R.A.S.* 336:785–796
156. Sesar B, Ivezić Ž, Grammer SH, Morgan DP, Becker AC, et al. 2010a.
Astrophysical Journal 708:717–741
157. Sesar B, Ivezić Ž, Jurić M. 2008. *Astrophysical Journal* 689:1244–1273
158. Sesar B, Ivezić Ž, Lupton RH, Jurić M, Gunn JE, et al. 2007.
Astronomical Journal 134:2236–2251
159. Sesar B, Jurić M, Ivezić Ž. 2011. *Astrophysical Journal* 731:4–+
160. Sesar B, Svilković D, Ivezić Ž, Lupton RH, Munn JA, et al. 2006.
Astronomical Journal 131:2801–2825
161. Sesar B, Vivas AK, Duffau S, Ivezić Ž. 2010b. *Astrophysical Journal* 717:133–139
162. Siebert A, Williams MEK, Siviero A, Reid W, Boeche C, et al. 2011.
Astronomical Journal 141:187–+

163. Siebert A, et al. 2008. *Monthly Notices of the R.A.S.* 391:793–801
164. Sirko E, et al. 2004. *Astronomical Journal* 127:914–924
165. Skrutskie MF, Cutri RM, Stiening R, Weinberg MD, Schneider S, et al. 2006. *Astronomical Journal* 131:1163–1183
166. Smith MC, Evans NW, Belokurov V, Hewett PC, Bramich DM, et al. 2009. *Monthly Notices of the R.A.S.* 399:1223–1237
167. Smith MC, Wyn Evans N, An JH. 2009. *Astrophysical Journal* 698:1110–1116
168. Smolinski JP, Lee YS, Beers TC, An D, Bickerton SJ, et al. 2011. *Astronomical Journal* 141:89–+
169. Soderblom DR. 2010. *Annu. Rev. Astro. Astrophys.* 48:581–629
170. Sommer-Larsen J, Götz M, Portinari L. 2003. *Astrophysical Journal* 596:47–66
171. Sommer-Larsen J, Zhen C. 1990. *Monthly Notices of the R.A.S.* 242:10–24
172. Springel V, Wang J, Vogelsberger M, Ludlow A, Jenkins A, et al. 2008. *Monthly Notices of the R.A.S.* 391:1685–1711
173. Starkenburg E, Helmi A, Morrison HL, Harding P, van Woerden H, et al. 2009. *Astrophysical Journal* 698:567–579
174. Steinmetz M, Navarro JF. 2002. *New Astronomy* 7:155–160
175. Steinmetz M, Zwitter T, Siebert A, Watson FG, Freeman KC, et al. 2006. *Astronomical Journal* 132:1645–1668
176. Twarog BA, Anthony-Twarog BJ. 1994. *Astronomical Journal* 107:1371–1380
177. van der Kruit PC, Freeman KC. 2011. *Annu. Rev. Astro. Astrophys.* 49:301–371
178. Vivas AK, Jaffé YL, Zinn R, Winnick R, Duffau S, Mateu C. 2008. *Astronomical Journal* 136:1645–1657

179. Vivas AK, Zinn R. 2006. *Astronomical Journal* 132:714–728
180. Vivas AK, Zinn R, Andrews P, Baily C, Baltay C, et al. 2001.
Astrophysical Journal Letters 554:L33–L36
181. Watkins LL, Evans NW, Belokurov V, Smith MC, Hewett PC, et al. 2009.
Monthly Notices of the R.A.S. 398:1757–1770
182. West AA, Hawley SL, Bochanski JJ, Covey KR, Reid IN, et al. 2008.
Astronomical Journal 135:785–795
183. Westerlund BE. 1990. *AAPR?* 2:29–78
184. Wetterer CJ, McGraw JT. 1996. *Astronomical Journal* 112:1046–+
185. Wilkinson MI, et al. 2005. *Monthly Notices of the R.A.S.* 359:1306–1335
186. Willman B. 2010. *Advances in Astronomy (also arXiv:0907.4758)*
187. Wilson ML, Helmi A, Morrison HL, Breddels MA, Bienaymé O, et al. 2011.
Monthly Notices of the R.A.S. 413:2235–2241
188. Wright EL, Eisenhardt PRM, Mainzer AK, Ressler ME, Cutri RM, et al. 2010.
Astronomical Journal 140:1868–1881
189. Wyse RFG. 2006. *Mem.S.A.It.* 77:1036–+
190. Xue XX, Rix HW, Yanny B, Beers TC, Bell EF, et al. 2011. *Astrophysical Journal*
738:79–+
191. Xue XX, et al. 2008. *Astrophysical Journal* 684:1143–1158
192. Yanny B, Newberg HJ, Grebel EK, Kent S, Odenkirchen M, et al. 2003.
Astrophysical Journal 588:824–841
193. Yanny B, Newberg HJ, Kent S, Laurent-Muehleisen SA, Pier JR, et al. 2000.
Astrophysical Journal 540:825–841

194. Yanny B, et al. 2009. *Astronomical Journal* 137:4377–4399
195. Yoachim P, Dalcanton JJ. 2006. *Astronomical Journal* 131:226–249
196. Yoachim P, Dalcanton JJ. 2008. *Astrophysical Journal* 682:1004–1019
197. York DG, et al. 2000. *Astronomical Journal* 120:1579–1587
198. Yoshii Y. 1982. *PASJ* 34:365–+
199. Zwitter T, Matijević G, Breddels MA, Smith MC, Helmi A, et al. 2010.
Astronomy & Astrophysics 522:A54+

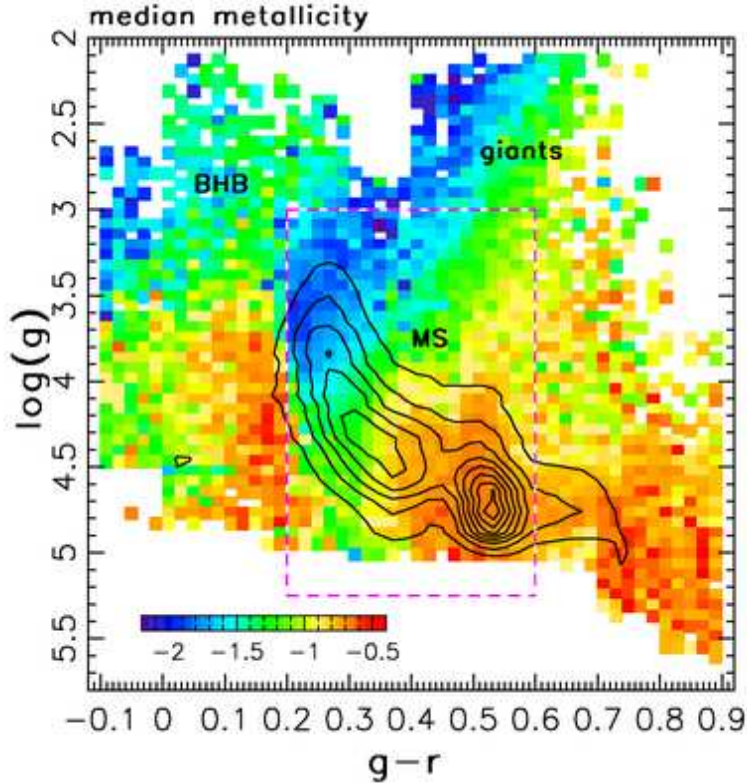


Figure 1: The stellar content of the SDSS spectroscopic surveys, through Data Release 6 (Figure 1 from Ivezić et al. 2008b). Linearly spaced contours show the distribution of $\sim 110,000$ stars with $g < 19.5$ and $0.1 < g-r < 0.9$ (corresponding to effective temperatures in the range $4500 \text{ K} < T_{\text{eff}} < 8200 \text{ K}$) in the $\log(g)$ vs. $g-r$ plane (g is the SDSS g -band magnitude, and $\log(g)$ measures the surface gravity). The multimodal distribution is a result of the SDSS target selection algorithm. The color scheme shows the median metallicity for all 0.02 mag by 0.06 dex pixels that contain at least 10 stars. The fraction of stars with $\log(g) < 3$ (giants) is 4%, and they are mostly found in two color regions: $-0.1 < g-r < 0.2$ (blue horizontal branch, BHB, stars) and $0.4 < g-r < 0.65$ (red giants). They are dominated by low-metallicity stars ($[Fe/H] < -1$). The dashed lines outline the main-sequence (MS) region, where photometric metallicity methods can be applied.

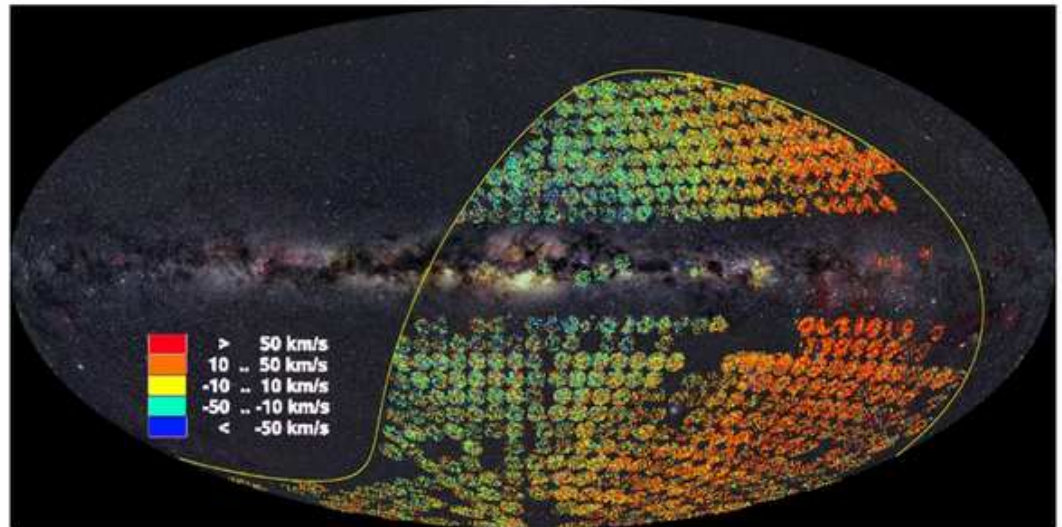


Figure 2: The sky coverage of RAVE DR3, shown as an Aitoff projection in Galactic coordinates and color-coded by the mean radial velocity (Figure 17 from Siebert et al. 2011). The nearly contiguous coverage over a wide solid angle, with detailed data for (eventually) up to a million stars is representative of modern Milky Way surveys and enables new approaches to studying the Galaxy. The distances probed by RAVE stars ranges up to ~ 1 kpc, thus the RAVE dataset provides a valuable link between the nearby Hipparcos sample (< 100 pc) and the more distant SDSS sample.

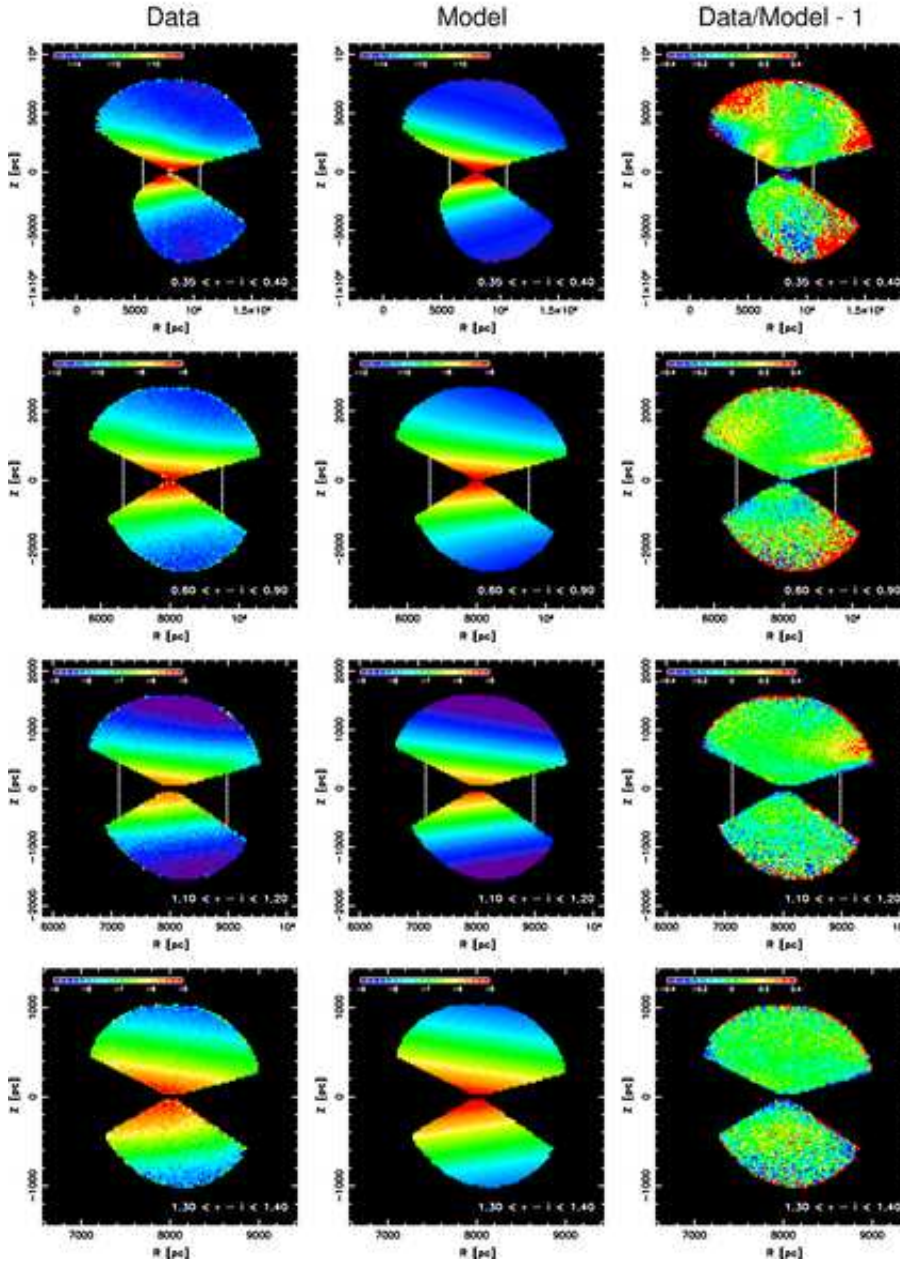


Figure 3: Figure 26 from Jurić et al. (2008). The panels in the left column show the measured stellar number density, as a function of Galactic cylindrical coordinates, for stars selected from narrow ranges of $r - i$ color ($0.35 < r - i < 0.40$ in the top row to $1.30 < r - i < 1.40$ in the bottom row). The panels in the middle column show the best-fit smooth models; panels in the right column show the normalized (data-model) difference map. Note the large overdensities visible in the top three panels in the right column.

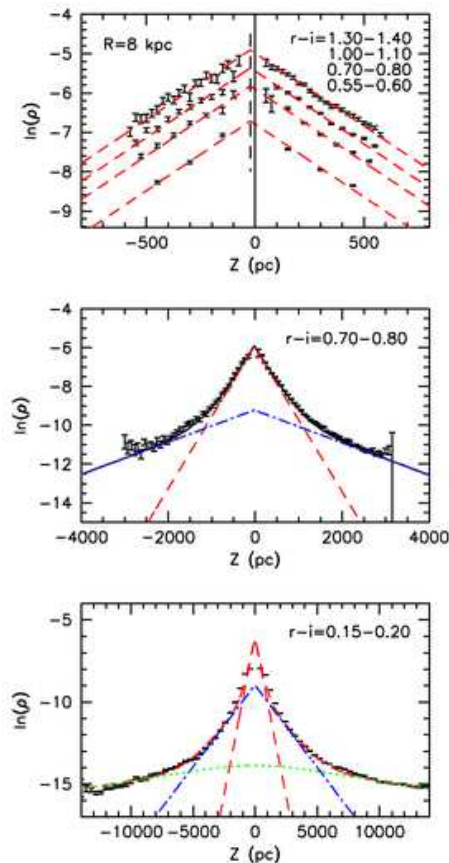


Figure 4: Cross sections through maps similar to those shown in Figure 3, showing the vertical ($|Z|$) distribution at $R = 8$ kpc and for different $r-i$ color bins (Figure 15 from Jurić et al. 2008). The lines are exponential models fitted to the points (the sech^2 function is not a good fit; see footnote 28 in Jurić08). The dashed lines in the top panel correspond to a fit with a single, exponential disk. The dashed line in the middle panel corresponds to a sum of two disks with scale heights of 270 pc and 1200 pc, respectively, and a relative normalization of 0.04 (the “thin” and the “thick” disks). The dashed line in the bottom panel (closely following the data points) corresponds to a sum of two disks and a power-law spherical halo. The dashed line and the dot-dashed line are the disk contributions, and the halo contribution is shown by the dotted line. For the best-fit parameters see Table 1.

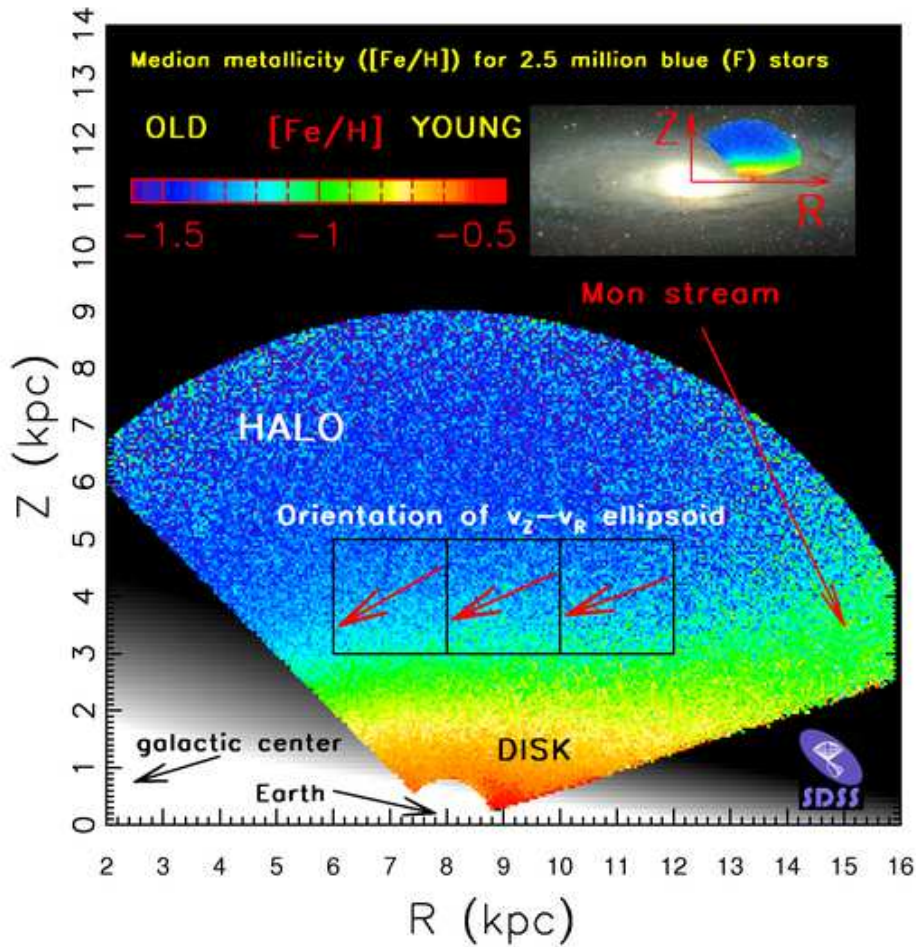


Figure 5: Variation of the median photometric stellar metallicity for ~ 2.5 million stars from SDSS with $14.5 < r < 20$ and $0.2 < g - r < 0.4$, and photometric distance in the 0.8-9 kpc range, in cylindrical Galactic coordinates R and $|Z|$ (adapted from Ivezić08). The $\sim 40,000$ pixels (50 pc by 50 pc) contained in this map are colored according to the legend in the top left. Note that the gradient of the median metallicity is essentially parallel to the $|Z|$ axis, except in the region of the Monoceros stream, as marked. The gray-scale background is the best-fit model for the stellar number-density distribution from Juric08. The inset in the top right illustrates the extent of the data volume relative to the rest of Galaxy; the background image is the Andromeda galaxy. The three squares outline the regions used to construct the $v_Z - v_R$ ellipsoids shown in Figure 16. The arrows illustrate the variation of the ellipsoid orientation, which always points towards the Galactic center.

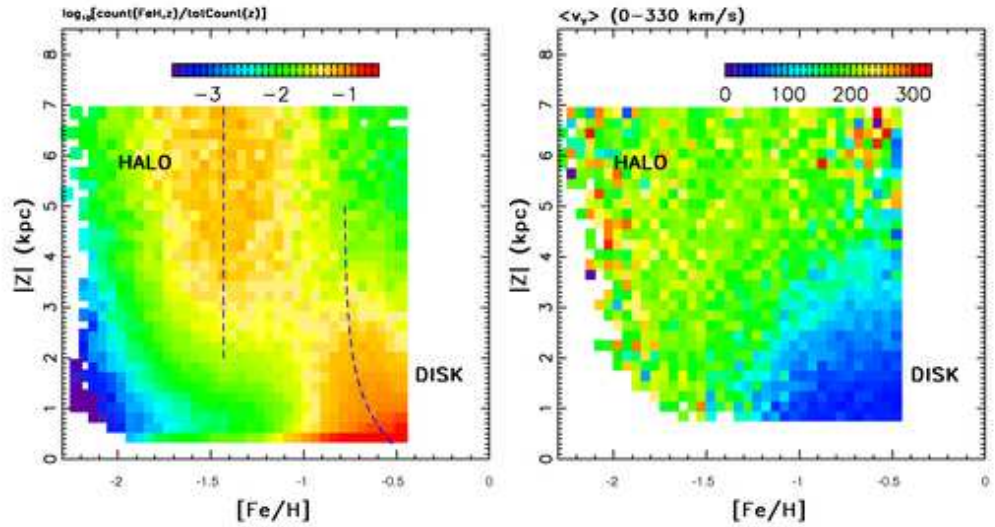


Figure 6: Figure 9 from Ivezić et al. (2008b). The left panel shows the conditional metallicity probability distribution (each row of pixels integrates to unity) for $\sim 60,000$ stars from a cylinder perpendicular to the Galactic plane, centered on the Sun, and with a radius of 1 kpc. The values are color coded on a logarithmic scale according to the legend on top. The lack of stars with $[Fe/H] > -0.5$ is due to a bias in SDSS Data Release 6 reductions, and an updated version of this map based on Data Release 7 is shown in Figure A.3 from Bond et al. (2010). The right panel shows the median heliocentric rotational velocity component (the value of $\sim 220 \text{ km s}^{-1}$ corresponds to no rotation), as a function of metallicity and distance from the Galactic plane, for the $\sim 40,000$ stars from the left panel that also satisfy $|b| > 80^\circ$.

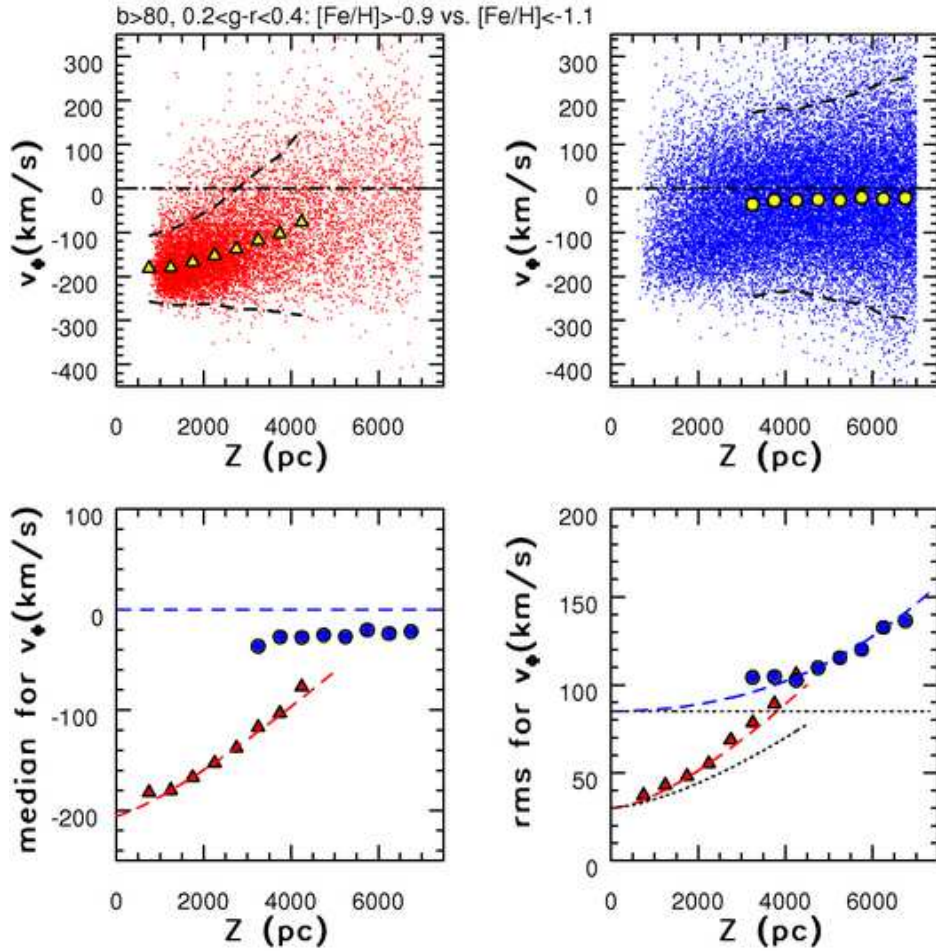


Figure 7: Figure 5 from Bond et al. (2010). A comparison of the variation of rotational velocity (see their eqn. 8), v_{ϕ} , on distance from the Galactic plane, $|Z|$, for 14,000 high-metallicity ($[Fe/H] > -0.9$; top left panel) and 23,000 low-metallicity ($[Fe/H] < -1.1$; top right panel) stars with $|b| > 80^\circ$. In the top two panels, individual stars are plotted as small dots, and the medians in bins of $|Z|$ are plotted as large symbols. The 2σ envelope around the medians is shown by dashed lines. The bottom two panels compare the medians (left) and dispersions (right) for the two subsamples shown in the top panels, and the dashed lines in the bottom two panels show predictions of a kinematic model. The dotted lines in the bottom-right panel show model dispersions (without correction for measurement errors).

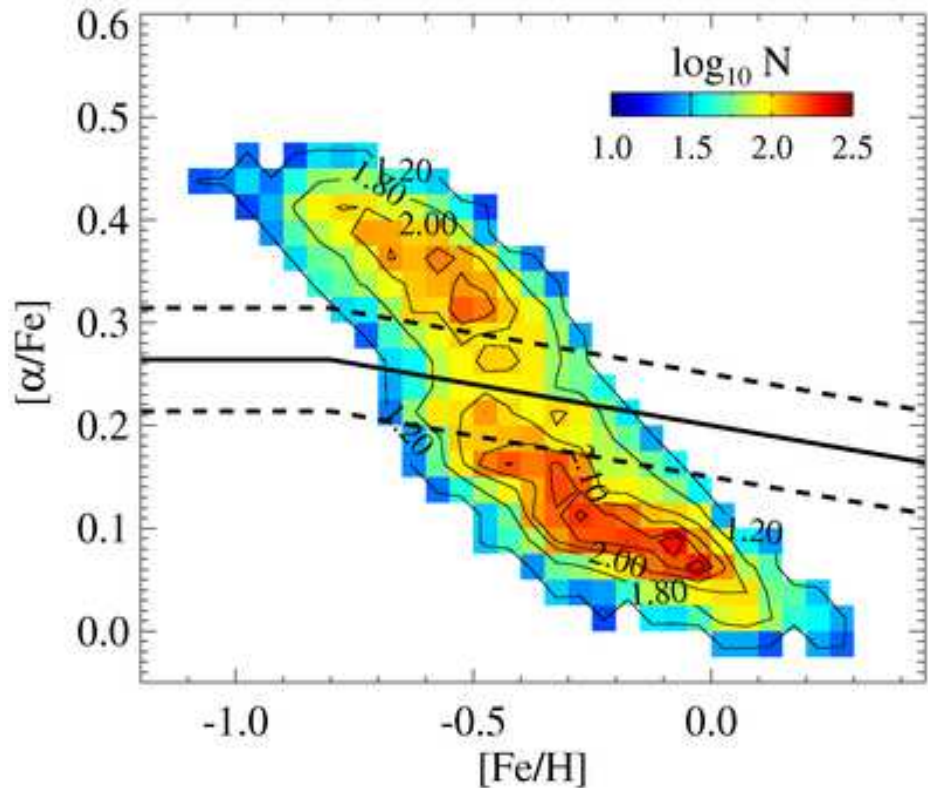


Figure 8: The $[\alpha/Fe]$ vs. $[Fe/H]$ distribution of G-type dwarfs within a few kpc from the Sun (Figure 2 from Lee et al. 2011b). The number density (arbitrarily normalized) is shown on a logarithmic scale according to the legend, and by isodensity contours. Each pixel (0.025 dex in the $[\alpha/Fe]$ direction and 0.05 dex in the $[Fe/H]$ direction) contains at least 20 stars (with a median occupancy of 70 stars). The distribution of disk stars in this diagram can be described by two components (thin disk and thick disk, respectively) centered on $([Fe/H], [\alpha/Fe]) = (-0.2, +0.10)$ and $(-0.6, +0.35)$. The solid line is the fiducial for division into likely thin- and thick-disk populations; note that a simple $[\alpha/Fe] = 0.24$ separation results in almost identical subsamples. The dashed lines show the selection boundaries adopted by Lee et al. (2011b), which exclude the central overlap region.

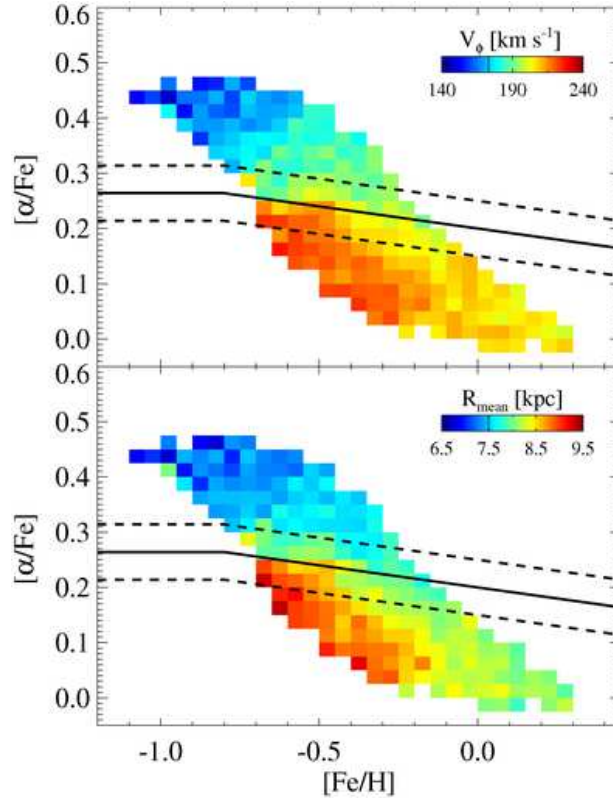


Figure 9: Distribution of mean rotational velocities (v_ϕ , top panel) and the orbital radii (R_{mean} , bottom panel) for the G-dwarf sample from Lee et al. (2011b; their Figure 5) in the $[\alpha/\text{Fe}]$ vs. $[\text{Fe}/\text{H}]$ diagram (3σ -clipped mean values). The orbital parameters are computed using an analytic Stäckel-type gravitational potential from Chiba & Beers (2000). The rotational velocity (v_ϕ) is defined in a left-handed coordinate system (the disk rotation is $+220 \text{ km s}^{-1}$). Note the rich structure present in both panels.

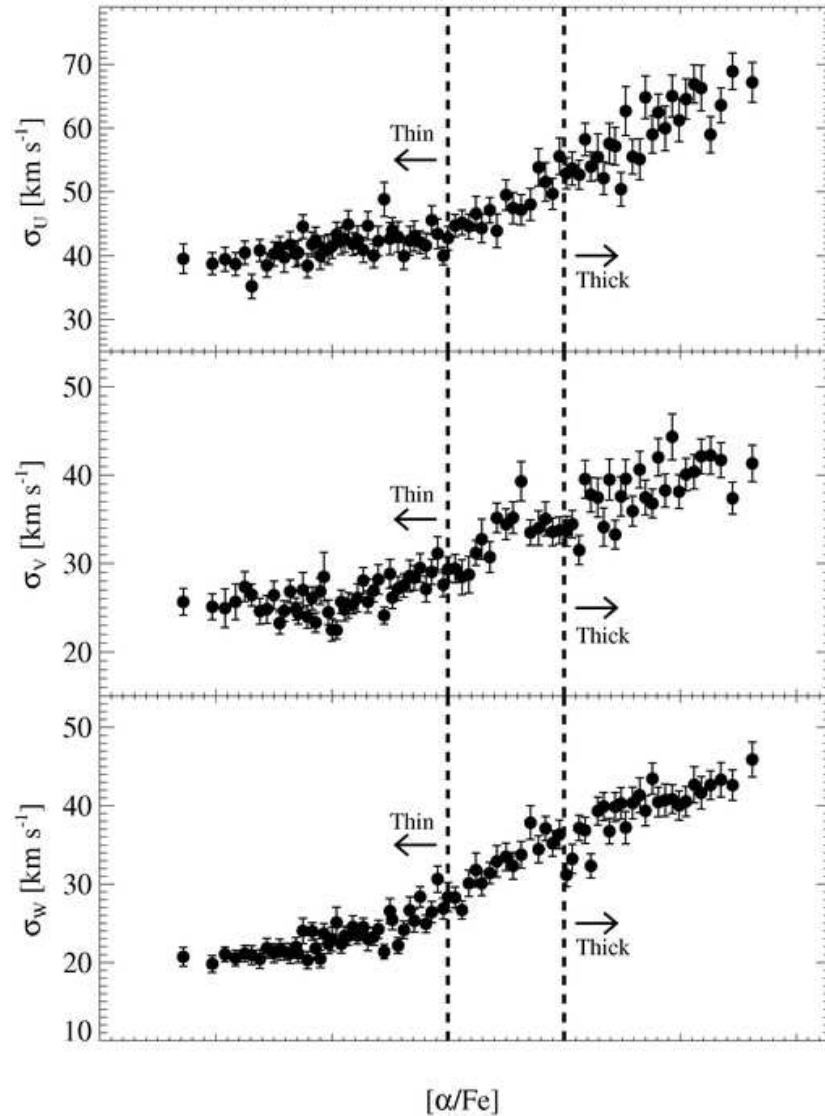


Figure 10: Variation of the three velocity dispersions with $[\alpha/Fe]$. (Figure 3 from Lee et al. 2011b). Each data point represents 200 stars and the error bars are calculated by the bootstrap method. The vertical dashed lines at $[\alpha/Fe] = +0.2$ and $+0.3$ are added to guide the eye, and roughly correspond to thin/thick disk separation. The easily discernible increase of all three velocity dispersions with $[\alpha/Fe]$ provides kinematics-based support for the chemical $[\alpha/Fe]$ -based separation of the two dominant disk components.

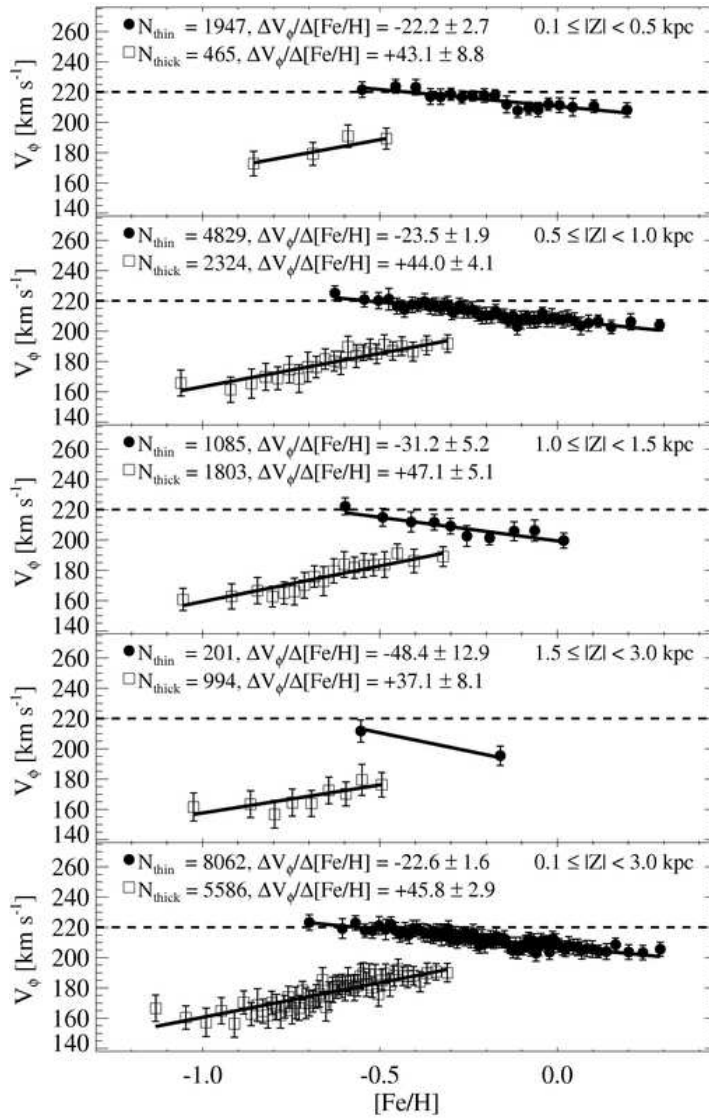


Figure 11: Variation of the mean rotational velocity of G-dwarf stars with metallicity for different slices in distance from the Galactic plane (top four panels), for stars separated using $[\alpha/\text{Fe}]$; thin-disk stars (black dots) and thick-disk stars (open squares) are shown (Figure 7 from Lee et al. 2011b). The rotational velocity (v_{Φ}) is defined in a left-handed coordinate system (the disk rotation is $+220 \text{ km s}^{-1}$). Each dot represents a 3σ -clipped average of 100 stars. The bottom panel shows the results for the full samples of stars considered. Estimates of the slopes and their errors listed in the panels are computed for unbinned data.

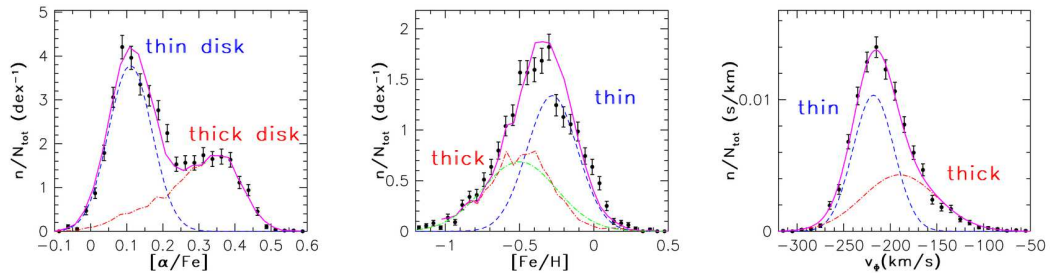


Figure 12: Tests of thin/thick-disk decomposition, using the sample of G-type dwarfs from Lee et al. (2011b). The left panel shows the $[\alpha/\text{Fe}]$ distribution for $\sim 2,300$ stars in the fiducial bin $|Z|=400\text{-}600$ pc as symbols with (Poissonian) error bars. The bimodality is easily seen. The observed distribution can be modeled as the sum (shown by the magenta solid line) of two components: the $[\alpha/\text{Fe}]$ distribution for $\sim 3,300$ stars with $|Z|=2\text{-}3$ kpc shifted to lower values by 0.03 dex (red dot-dashed line) and a Gaussian distribution, $N(0.11, 0.06)$ (blue dashed line). The weights for the two components (0.43 and 0.57, for the thick and thin component, respectively) are consistent with a double-exponential fit to star counts. The middle panel shows the $[\text{Fe}/\text{H}]$ distribution for the same stars from the fiducial $Z=400\text{-}600$ pc bin as symbols with error bars. Similar to the $[\alpha/\text{Fe}]$ distribution, it can be modeled as the sum (magenta solid line) of two components: the $[\text{Fe}/\text{H}]$ distribution for stars with $|Z|=2\text{-}3$ kpc shifted to higher values by 0.2 dex (jagged red dot-dashed line) and $N(-0.28, 0.17)$ (blue dashed line). The weights for the two components (0.43 and 0.57) are the same as in the first panel. The $[\text{Fe}/\text{H}]$ distribution for stars with $|Z|=2\text{-}3$ kpc is well described by $N(-0.50, 0.25)$ (after application of a 0.2 dex offset), shown as the smooth green dot-dashed line. The right panel shows the rotational velocity distribution for the same stars from the fiducial $|Z|=400\text{-}600$ pc bin as symbols with error bars. It can be modeled as a linear combination of two Gaussian distributions, $N(-218, 22)$ and $N(-190, 40)$, again using the same relative weights (and line styles) as in the first panel.

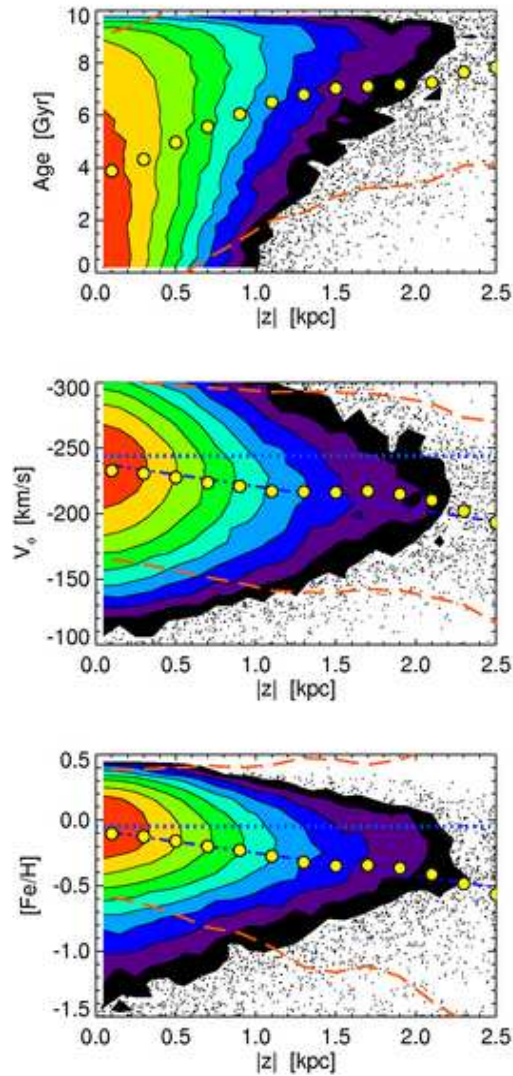


Figure 13: Predictions of the radial-migration model from Roškar et al. (2008b) for the variation of stellar age, rotational velocity, and metallicity with distance from the Galactic plane for stars in the solar cylinder (Figure 8 from Loebman et al. 2011). The simulated distributions are represented by color-coded contours (low to medium to high: black to green to red) in the regions of high density, and as individual points otherwise. The large symbols show the means for the $|Z|$ bins, and the dashed lines show a 2σ envelope. The gradients seen in the bottom two panels are consistent with the SDSS-based results.

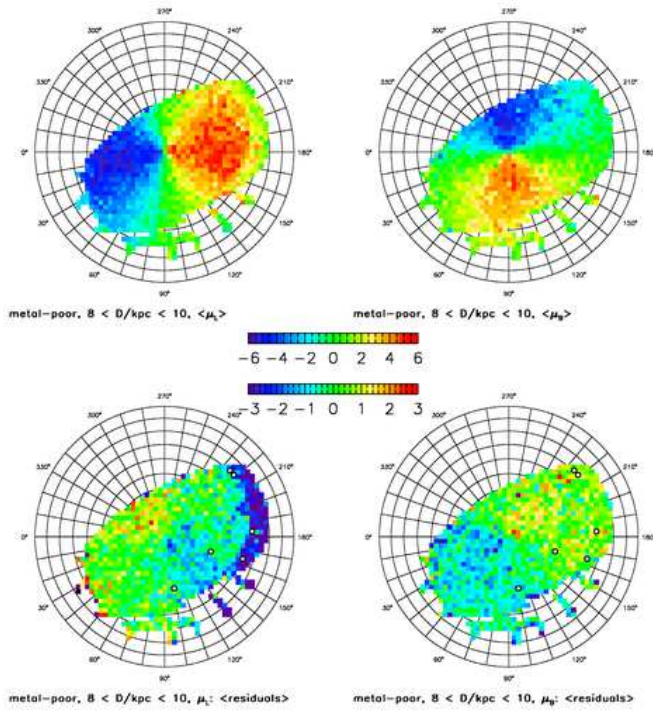


Figure 14: Figure 21 from Bond et al. (2010). Distribution of the median longitudinal proper motion in a Lambert projection of the North Galactic cap for low-metallicity (spectroscopic $[Fe/H] < -1.1$), blue ($0.2 < g - r < 0.4$) stars, with distances in the range 8-10 kpc. The top two panels show the median longitudinal (left) and latitudinal (right) proper motions, and the two bottom panels show the median difference between the observed and model-predicted values. The maps are color-coded according to the legends in the middle (mas yr^{-1}); note that the bottom scale has a harder stretch to emphasize structure in the residual maps). In the bottom panels, the white symbols show the positions of the six northern cold substructures (see §6.4) identified by Schlafman et al. (2009).

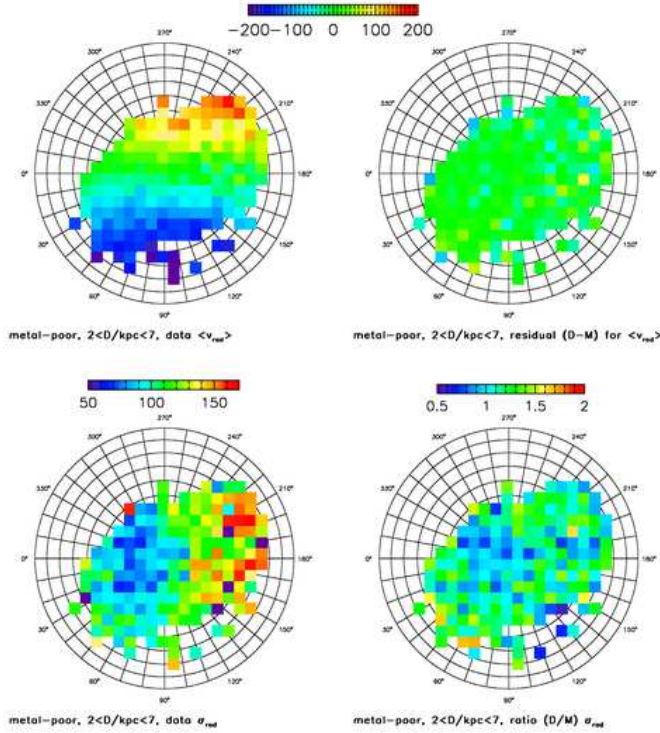


Figure 15: Figure 16 from Bond et al. (2010). Comparison of medians and dispersions for the measured and modeled radial velocities of 20,000 blue ($0.2 < g - r < 0.4$) halo stars (spectroscopic $[Fe/H] < -1.1$) at distances $D = 2 - 7$ kpc, and $b > 20^\circ$. The top-left panel shows the median measured radial velocity in each pixel, color-coded according to the legend shown at the top (units are km s^{-1}). The top-right panel shows the difference between this map and an analogous, visually similar, map based on model-generated values of radial velocity, using the same scale as in the top-left panel. The bottom-left panel shows the dispersion of measured radial velocities, color-coded according to the legend above it. The bottom-right panel shows the ratio of this map and an analogous, visually similar, map based on model-generated values of radial velocity, color-coded according to the legend above it.

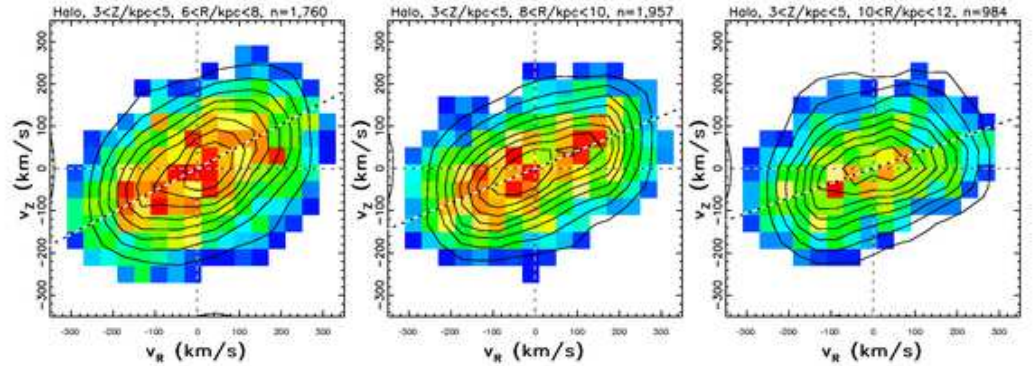


Figure 16: Figure 13 from Bond et al. (2010). The two-dimensional v_Z vs. v_R projections of the velocity distribution for three subsamples of candidate halo stars selected using spectroscopic metallicity ($-3 < [Fe/H] < -1.1$), with $3 < |Z|/\text{kpc} < 5$, and $6 < R/\text{kpc} < 8$ (left), $8 < R/\text{kpc} < 10$ (middle), and $10 < R/\text{kpc} < 12$ (right). These $R - Z$ boundaries are illustrated in Figure 5. The distributions are shown using linearly spaced contours, and with a color-coded map showing smoothed counts in pixels (low to high from blue to red). The measurement errors are typically 60 km s^{-1} , and the dashed lines show the median direction toward the Galactic center. Note the strong evidence for a velocity-ellipsoid tilt, and the variation of the tilt with R , so that the ellipsoid always points towards the Galactic center.

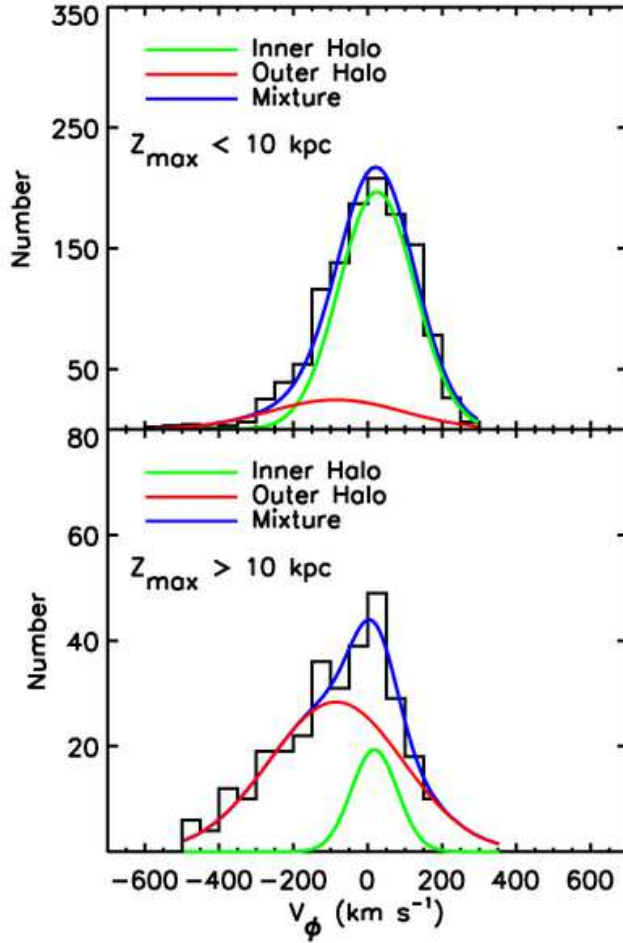


Figure 17: Rotational properties for the low-metallicity ($[Fe/H] < -2.0$) subsample of SDSS calibration stars, divided into stars with maximum orbital distances from the plane (Z_{max}) above or below 10 kpc (Figure 10 from Carollo et al. 2010). The histograms show the observed distribution of rotational velocity (v_ϕ), and the smooth curves show models for the inner (green) and outer (red) halo components (the model sum is shown by the blue curves).

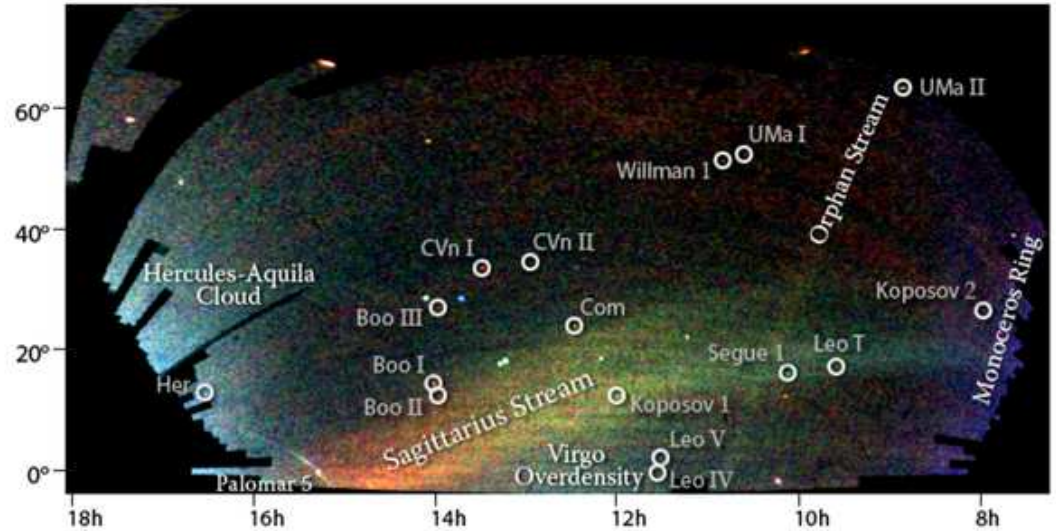


Figure 18: The “Field of Streams” map of blue stars in the outer regions of the Milky Way, derived from the SDSS images of the northern sky, shown in a Mercator-like projection of equatorial coordinates (based on Figure 1 from Belokurov et al. 2006a; courtesy of V. Belokurov, Institute of Astronomy, Cambridge). The color indicates the distance of the stars (of the order 10 kpc), with red being the most distant and blue being the closest, while the intensity indicates the density of stars on the sky. There are several structures visible in this map, as marked, that demonstrate the halo is not a smooth structure. Circles enclose new Milky Way companions discovered by the SDSS, as labeled; two of these are faint globular star clusters, while the others are faint dwarf galaxies.

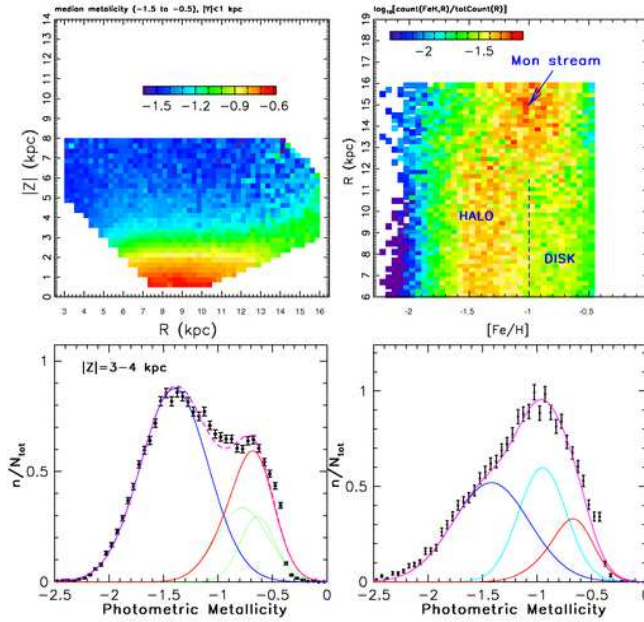


Figure 19: Figure 18 from Ivezić et al. (2008b). Top left panel: Dependence of the median photometric metallicity for one million stars with $14.5 < r < 20$, $0.2 < g - r < 0.4$, and $|Y| < 1$ kpc, in cylindrical Galactic coordinates R and $|Z|$. This Y range is selected to include the Monoceros stream, which represents an overdensity by a factor of ~ 1.5 in a region around $R \sim 15$ kpc and $|Z| \sim 3 - 4$ kpc. As discernible from the map, this region has a larger median metallicity than expected for this $|Z|$ range based on extrapolation from smaller R . Top right panel: Conditional metallicity probability distribution for a subsample of $\sim 111,000$ stars with $3 < |Z|/\text{kpc} < 4$. The strong overdensity at $R > 12$ kpc is the Monoceros stream. The bottom panels show the metallicity distribution (symbols with error bars) for a subsample of $\sim 40,000$ stars with $6 < R/\text{kpc} < 9$ (left) and for $\sim 12,000$ stars with $13 < R/\text{kpc} < 16$ (right). The lines represent empirical fits based on Gaussian decomposition from Ivezić et al. (2008b) (blue lines for halo component and red lines for disk component). The cyan line in the bottom right panel is a 0.22 dex wide Gaussian centered on $[Fe/H] = -0.95$. It accounts for 33% of stars in the sample that presumably belong to the Monoceros stream.

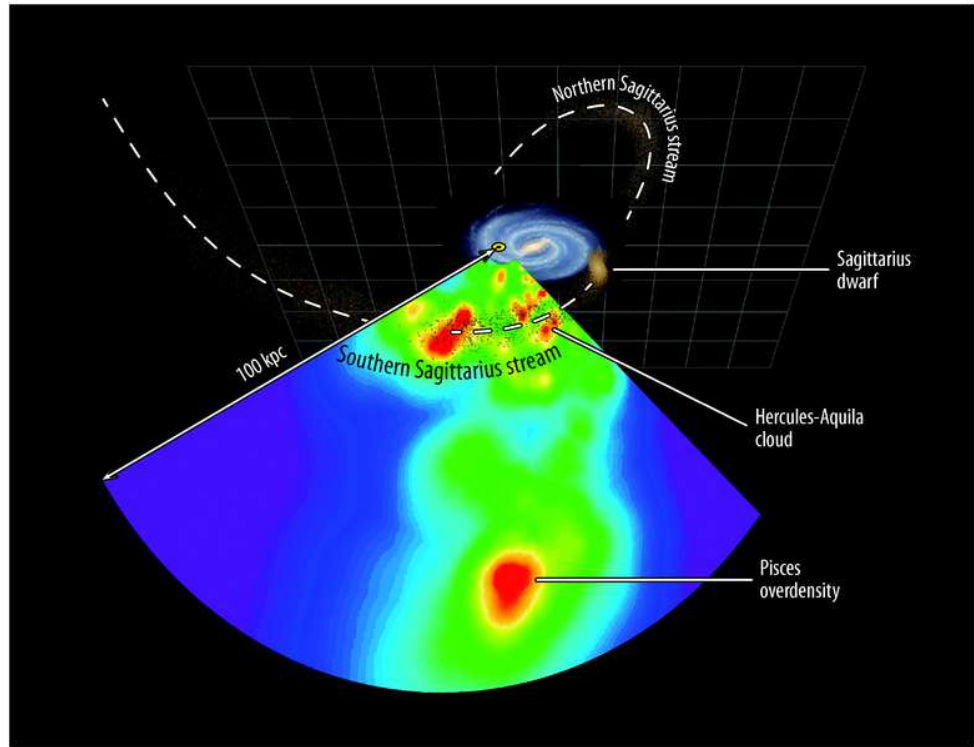


Figure 20: The distribution of RR Lyrae stars from SDSS Stripe 82, contrasted with an artist’s concept of the disk plane (based on Figure 12 from Sesar et al. 2010a). The color scheme displays the RR Lyrae number density multiplied by the cube of the Galactocentric radius (logarithmic scale, from light blue to red). Note the rich structure present. The white dots, outlined by white dashed lines, show the Sagittarius dSph (“Sgr dwarf”) and its tidal streams, as modeled by the Law, Johnston & Majewski (2005) “spherical” model (the model stream overlaps with one of the detected clumps, “Sgr for discussion see Sesar et al. 2010a). An animated version is available from the ARA&A website (courtesy of A. Mejia and B. Sesar).

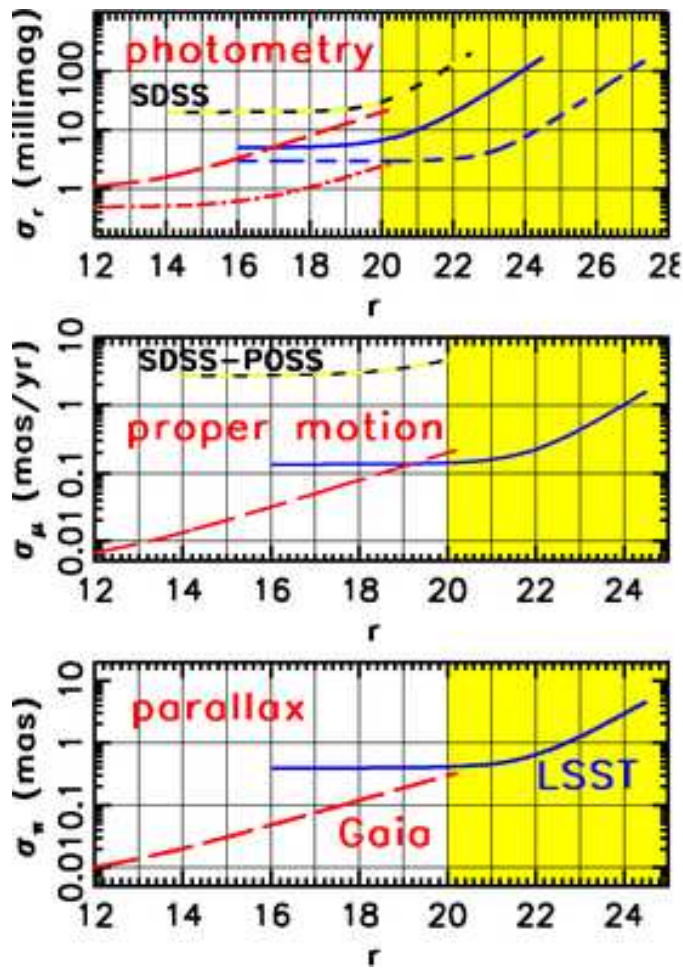


Figure 21: A comparison of the photometric, proper-motion, and parallax errors for SDSS, Gaia, and LSST, as a function of apparent magnitude r , for a G2V star (Eyer et al, in prep). In the top panel, the curve marked “SDSS” corresponds to a single SDSS observation. The red curves correspond to Gaia; the long-dashed curve shows a single-transit accuracy, while the dot-dashed curve shows the end-of-mission accuracy (assuming 70 transits). The blue curves correspond to LSST; the solid curve shows a single -visit accuracy, while the short-dashed curve shows the accuracy for co-added data (assuming 230 visits in the r -band). The curve marked “SDSS-POSS” in the middle panel shows the accuracy delivered by the proper-motion catalog of Munn et al. (2004).

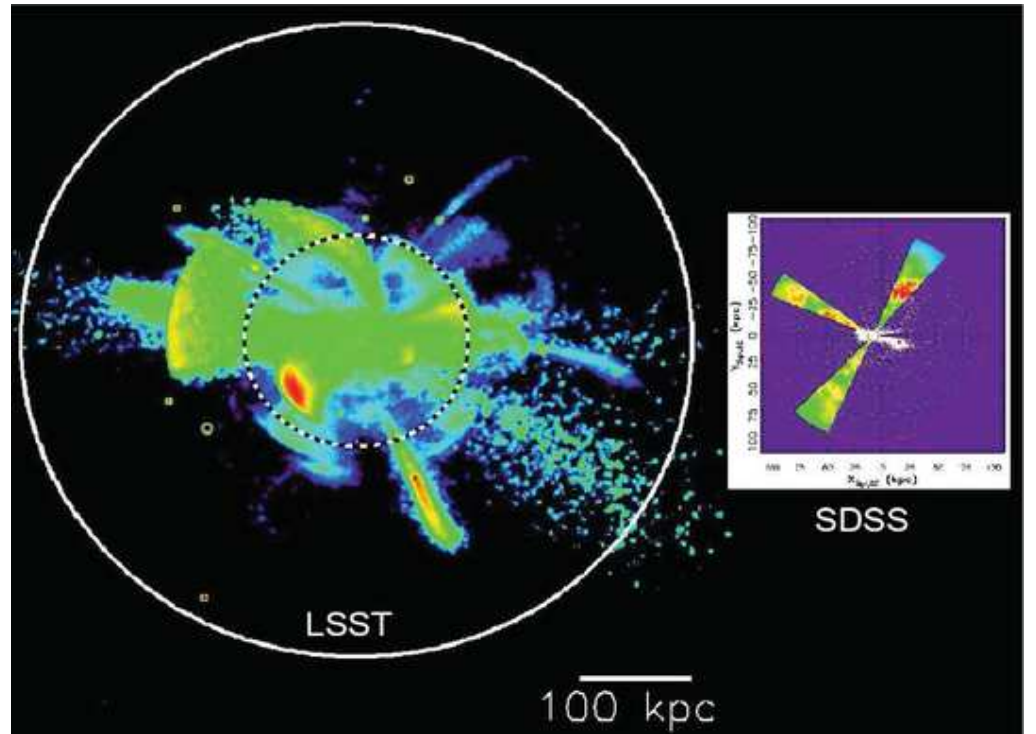


Figure 22: A simulation of the outer regions of the Milky Way (left), compared to the current state-of-the-art data (right), shown on the same spatial scale. The data panel presents the number density multiplied by the cube of the Galactocentric radius (logarithmic scale with dynamic range of 1000, from blue to red), for ~ 1000 SDSS RR Lyrae stars within 10° of the Sgr dwarf tidal stream plane (Ivezić et al. 2004). The same color coding was used to visualize the stellar number density for a Milky Way-type galaxy simulation from Bullock & Johnston (2005), shown on the left. Set within an Λ CDM merger history, these simulations track the accretion and disruption of hundreds of dwarf galaxies into Milky-Way size halos. With LSST, RR Lyrae stars will be found beyond the presumed Milky Way tidal radius (~ 300 kpc, white circle), and the much more numerous main-sequence stars will trace the structure out to 100 kpc (dashed circle). The latter distance range can at present only be probed using RR Lyrae stars and other rare non-main-sequence stars.

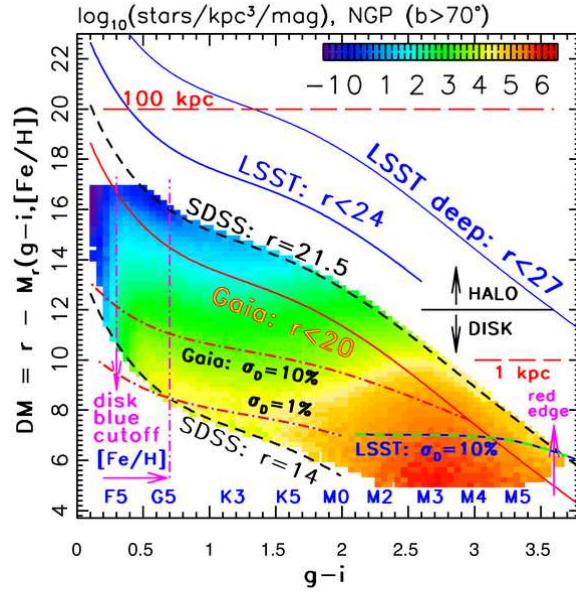


Figure 23: The volume number density (stars/kpc³/mag, log scale according to the legend) of main-sequence stars with $14 < r < 21.5$ and $b > 70^\circ$, as a function of their distance modulus and $g - i$ color (based on SDSS data). The absolute magnitudes are determined using the photometric parallax relation from Ivezić08. The MK spectral type is indicated above the $g - i$ axis. The two vertical arrows mark the turn-off color for disk stars and the red edge of the M-dwarf color distribution. The $[Fe/H]$ label shows the color range ($g - i < 0.7$) where the photometric metallicity estimator from Ivezić08 performs best. The two diagonal dashed lines, marked $r = 14$ and $r = 21.5$, show the apparent magnitude limits for SDSS data. The diagonal solid lines mark the apparent magnitude limits for Gaia ($r < 20$), LSST’s single-epoch data ($r < 24$, 10σ), and LSST’s stacked data ($r < 27$, 10σ). The dashed line in the lower right corner marks the distance limits for obtaining 10% accurate trigonometric distances using LSST data. The two dot-dashed lines mark analogous limits for obtaining 1% and 10% accurate trigonometric distances using Gaia’s data.